

Time-optimal Convexified Reeds-Shepp Paths on a Sphere

Sixu Li, *Student Member, IEEE*, Deepak Prakash Kumar, *Student Member, IEEE*, Swaroop Darbha, *Fellow, IEEE*, Yang Zhou, *Member, IEEE*

Abstract—This article addresses time-optimal path planning for a vehicle capable of moving both forward and backward on a unit sphere with a unit maximum speed, and constrained by a maximum absolute turning rate U_{max} . The proposed formulation can be utilized for optimal attitude control of underactuated satellites, optimal motion planning for spherical rolling robots, and optimal path planning for mobile robots on spherical surfaces or uneven terrains. By utilizing Pontryagin’s Maximum Principle and analyzing phase portraits, it is shown that for $U_{max} \geq 1$, the optimal path connecting a given initial configuration to a desired terminal configuration falls within a sufficient list of 23 path types, each comprising at most 6 segments. These segments belong to the set $\{C, G, T\}$, where C represents a tight turn with radius $r = \frac{1}{\sqrt{1+U_{max}^2}}$, G represents a great circular arc, and T represents a turn-in-place motion. Closed-form expressions for the angles of each path in the sufficient list are derived. The source code for solving the time-optimal path problem and visualization is publicly available at <https://github.com/sixuli97/Optimal-Spherical-Convexified-Reeds-Shepp-Paths>.

Index Terms—Reeds-Shepp vehicle, time-optimal paths, optimization and optimal control, spherical path planning, space robotics, spherical rolling robot.

I. INTRODUCTION

AUTONOMOUS vehicles and robotics have seen significant advancements and applications recently, creating a growing demand for effective path planning across diverse scenarios. In the realm of path planning, time-optimal paths hold significant value because they offer a fundamental metric on the configuration space [1]. Additionally, they act as effective motion primitives [2], [3], which can be sampled or sequentially combined to tackle more complex tasks like avoiding obstacles. Typically, time-optimal path planning problems in a plane aim to find the path with the shortest time that connects an initial configuration¹ to a desired terminal configuration of a vehicle. The vehicle is modeled as a rigid body with kinematic constraints. In [4], such a problem was solved for a forward-moving vehicle with constant speed $v = 1$, and bounded turning rate² $u \in [-U_{max}, U_{max}]$, which is known as the Dubins vehicle. The authors proved that the optimal

path must be of types CCC , CSC , or their degenerate forms, where C represents a left or right turn with a maximum turning rate and S denotes a straight line. In [5], the problem was extended to the Reeds-Shepp (RS) vehicle, which moves both forward and backward with $v \in \{-1, 1\}$. It was proven that the optimal path of an RS vehicle must be one of the following types: CSC , $C|C|C$, $CC|C$, $C|CC$, $CC|CC$, $C|CC|C$, $C|CSC$, $CSC|C$, $C|CSC|C$, or its degenerate form; here, “|” represents a cusp.

The aforementioned pioneering works relied on geometry and differential calculus. Subsequent improvements to the RS results were made using the Pontryagin Maximum Principle (PMP) [6], as seen in [7] and [8]. In particular, [8] addressed the RS problem by relaxing the constraint $v \in \{-1, 1\}$ to $v \in [-1, 1]$, resulting in a convexified version known as the convexified Reeds-Shepp (CRS) problem. The authors showed that, in a plane, the sufficient list of time-optimal paths for the CRS problem is also admissible for the RS problem, indicating that the sufficient lists for both problems are identical. Later, in [9], it was proved that the sufficient lists for the time-optimal CRS problem and the minimum wheel-rotation differential-drive problem also coincide. A phase portrait approach was recently used in [10] for obtaining a simplified proof utilizing PMP; this approach resembles the approach of [11] for the non-Euclidean Dubins’ problem. A similar phase-portrait approach was used to solve the weighted Dubins problem using PMP in [12]. Time-optimal paths of differential drive vehicles, omni-directional vehicles, and car-like mobile robots in a plane were studied using PMP in [13], [1], and [14], respectively.

Although optimal path planning in 3D has posed difficulties, there exist several significant studies in the field. In [15], the problem of a 3D Dubins path with constraints on total curvature was investigated, demonstrating that the time-optimal path is either a helicoidal arc or composed of up to three segments. However, this study does not take into account the full configuration of the vehicle in 3D space. In [16], the Dubins vehicle model was extended to incorporate altitude, allowing for the modeling of airplanes. The study determined the time-optimal paths for achieving final altitudes categorized as low, medium, and high. Nevertheless, the full configuration space was not comprehensively considered, and the challenges for control synthesis remained open. For surfaces of non-negative curvature, the existence conditions of Dubins paths were given in [17] without addressing the optimality of the paths. Exploring optimal paths on a sphere is another valuable area, particularly due to its relevance in path planning on uneven terrain and planetary surfaces, as well as in attitude

(Corresponding authors: Swaroop Darbha, Yang Zhou)

Sixu Li and Yang Zhou are with the Zachry Department of Civil & Environmental Engineering, Texas A&M University, College Station, TX 77843, USA (e-mail: sixuli@tamu.edu; yangzhou295@tamu.edu).

Deepak Prakash Kumar and Swaroop Darbha are with the Department of Mechanical Engineering, Texas A&M University, College Station, TX 77843 USA (e-mail: deepakprakash1997@gmail.com; dswaroop@tamu.edu).

¹The configuration of a vehicle is defined by its position and orientation.

²With a constant speed, a bounded turning rate corresponds to a minimum turning radius.

control. In [11], it was shown that the results of planar Dubins generalize to a unit sphere for the specific value $r = \frac{1}{\sqrt{2}}$ (or $U_{max} = 1$), where $r = \frac{1}{\sqrt{1+U_{max}^2}}$ denotes the radius of the tight turn. In [18], the spherical Dubins problem was studied for $r \leq \frac{1}{2}$ (or $U_{max} \geq \sqrt{3}$) by modeling the vehicle using a Sabban frame and constructing a geodesic curvature-constrained time-optimal path problem. The authors proved that for $r \leq \frac{1}{2}$, the optimal path is of types CCC , CGC , or their degenerate forms, where C represents a left or right turn with the maximum absolute geodesic curvature, and G denotes a great circular arc on the sphere—a geodesic. In [19], the spherical Dubins problem was extended to free terminal orientation using PMP. The authors proved that for $r \leq \frac{\sqrt{3}}{2}$ (or $U_{max} \geq \frac{1}{\sqrt{3}}$), the time-optimal paths must be of types CG , CC , or their degenerate forms.

However, from the surveyed papers, the Dubins vehicle is the only vehicle for which optimal paths on a sphere have been studied. In this paper, we extend this exploration to the spherical CRS problem. As depicted in Fig. 1, the configuration of a CRS vehicle on a sphere is represented by a collection of vectors $\mathbf{X}_v(t)$, $\mathbf{T}_v(t)$, and $\mathbf{N}_v(t)$, which denote the CRS vehicle's position, heading direction, and lateral direction, respectively. The spherical CRS problem involves finding a path that starts from an initial configuration $[\mathbf{X}_v(0), \mathbf{T}_v(0), \mathbf{N}_v(0)]$ at $t = 0$, and reaches a desired terminal configuration $[\mathbf{X}_v(T), \mathbf{T}_v(T), \mathbf{N}_v(T)]$ at $t = T$, while minimizing T . The CRS vehicle is subjected to the input constraints $u_g(t) \in [-U_{max}, U_{max}]$ and $v(t) \in [-1, 1]$. Here, u_g represents the turning rate, dictating the CRS vehicle's ability to turn away from its heading direction $\mathbf{T}_v(t)$, while v denotes the vehicle's speed, determining its ability to move along $\mathbf{T}_v(t)$. Fig. 2(a) shows fixed-time paths with a fixed speed $v = 1$ and various constant values of u_g . Since v is fixed, the arc lengths of the paths are identical, but the change in heading increases as $|u_g|$ increases. Fig. 2(b) shows fixed-time paths with a fixed turning rate $u_g = U_{max}$ and various constant values of v . Since u_g is fixed, the heading change remains the same across paths, while the arc length increases as $|v|$ increases. It is worth noting that there is no loss of generality in considering a unit maximum $|v|$ and a unit sphere since the distance and time can be scaled.

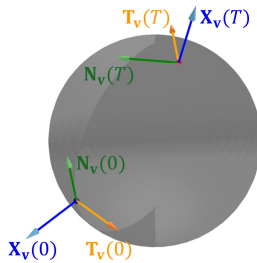


Fig. 1. Configurations on a sphere

The spherical CRS problem is motivated by three primary types of real-world applications:

1) *Optimal attitude control of underactuated satellites*: In scenarios where actuators fail, a satellite could become underactuated [20]; research from [21]–[23] shows that only

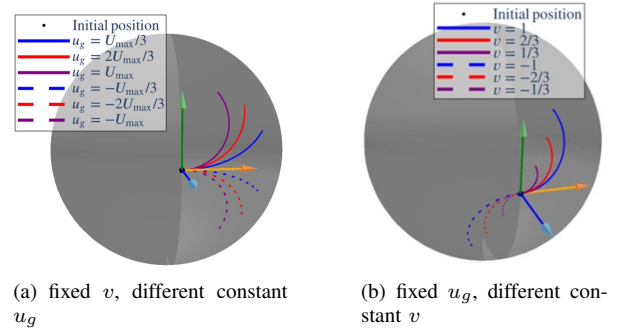


Fig. 2. Illustration of u_g and v

two control inputs suffice to control the pose of a satellite. The spherical CRS model is equivalent to the satellite model featuring two reaction wheels [24], [25]. This equivalence will be shown in more detail in Remark 2 in Section II. This work distinguishes from earlier work in the following two aspects: (1) the objective is to minimize the time to change pose with limited control effort, and (2) it is assumed that the reaction wheels' angular velocities are controlled instantaneously; therefore, this study can be considered as the development of a planner that produces a time-optimal trajectory, including references for both the satellite's pose and higher-level control signals, which can subsequently be tracked by a lower-level controller.

2) *Optimal motion planning for spherical rolling robots [26] with an internal drive unit (IDU)*. These robots possess a spherical outer shell with the IDU placed at the bottom inside. The IDU typically includes a unicycle maintaining continuous contact with the inner surface of the shell [27]–[29]. By controlling wheel rotation and direction, the IDU induces the shell to roll. Fig. 3 illustrates such a robot schematically. The kinematics of the shell's pose relative to the IDU [28], [29] is equivalent to the spherical CRS model, which describes the model of a CRS vehicle traveling on a unit sphere. This equivalence will be shown in more detail in Remark 3 in Section II. The model helps to perform motion planning tasks. For example, in reconnaissance, a shutter is incorporated into the shell, which allows sensors to extend outward [30]. The robot typically needs to reorient to position the shutter on top before extending the sensors. Assuming the wheels do not slip inside the shell and the ground friction is low, the shell-ground contact point will eventually be where the IDU comes to a stop on the shell. Hence, re-adjusting the shutter position can be achieved by directing the IDU to the shutter's antipodal point, as shown in Fig. 4. The dashed line from the shutter to the IDU's target runs through the sphere's center, with the red line showing the IDU's optimal path on the sphere.

3) *Optimal path planning for a CRS-like robot (e.g., with differential drive) on spherical surfaces or uneven terrains*. The application on spherical surfaces is straightforward and is utilized in inspection tasks (e.g., for spherical gas tanks [31], [32]). As for uneven terrains, the proposed formulation applies particularly to terrains that can be locally approximated by a spherical patch through curvature matching, indicating that the local terrain has nearly constant or gradually varying non-

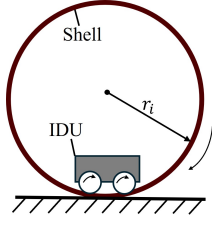


Fig. 3. Schematic plot of the spherical rolling robot

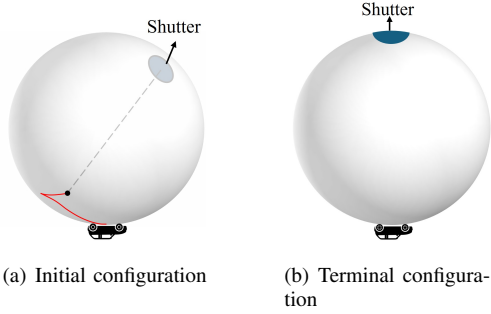


Fig. 4. Repositioning of the shutter

negative Gaussian curvature. Such terrain characteristics are seen in “gently rolling terrain”, as illustrated, for example, in Figure 2 of [33] and Figure 1 of [34]. Fig. 5 demonstrates such local approximation with a spherical patch, where the red line shows the optimal CRS path on the sphere. For a given start/terminal configuration pair, the set of all admissible paths on the spherical patch is contained within the set of all admissible paths on the entire sphere. Consequently, the path in Fig. 5 is also optimal within the patch. The difference between the actual terrain and its spherical patch approximation can be treated as a disturbance input to the lower-level controller.

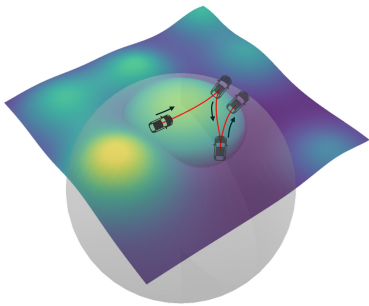


Fig. 5. Approximating local uneven terrain with a spherical patch

Another motivating factor is the exploration of mechanism design [1], [13]. Expanding the set of vehicles with known optimal paths enables direct comparisons between different actuation models. For example, in a robotic task that requires traveling between two configurations on a sphere in minimum time, we can evaluate whether a Dubins-type vehicle or a CRS-type vehicle³ is more efficient, while also considering

³A Dubins-type vehicle is equipped with a single controllable actuator, whereas a CRS-type vehicle is equipped with two controllable actuators.

trade-offs between travel time, actuation complexity, and implementation cost.

The main contributions of this paper are as follows:

- 1) Formulation of the spherical CRS problem.
- 2) Deriving necessary conditions of time-optimal paths using PMP and phase portraits.
- 3) Characterization of a sufficient list of the time-optimal path types for $U_{max} \geq 1$ by proving that some paths satisfying the necessary conditions are non-optimal or redundant.
- 4) Derivation of closed-form expressions for the angles of each path in the sufficient list, given an initial configuration, a desired terminal configuration, and U_{max} .
- 5) Full release of the source code for the research community to utilize, enhance, and build upon.

The remainder of this article is structured as follows. Section II presents the problem formulation and utilizes PMP to obtain some basic properties. Section III further characterizes the optimal paths and demonstrates that the problem can be divided into three distinct cases. These cases are analyzed in detail in Sections IV, V, and VI, respectively, obtaining a sufficient list of optimal path types. Section VII includes a discussion on path generation, along with a numerical example of solving the time-optimal path problem. Conclusions are drawn in Section VIII.

II. PROBLEM FORMULATION

In this section, the problem formulation is proposed, and PMP is utilized to obtain some basic properties of the optimal path.

In this paper, the time-optimal path of a CRS vehicle on a sphere is considered. The problem is modeled based on the spherical Dubins vehicle model using a Sabban frame, as proposed in [18]:

$$\begin{aligned} \frac{d\mathbf{X}}{ds} &= \mathbf{T}(s), & \frac{d\mathbf{T}}{ds} &= -\mathbf{X}(s) + u_g(s)\mathbf{N}(s), \\ \frac{d\mathbf{N}}{ds} &= -u_g(s)\mathbf{T}(s), \end{aligned} \quad (1)$$

where $\mathbf{X}, \mathbf{T}, \mathbf{N}$ denote the position vector, tangent vector, and the tangent-normal vector, respectively, and form an orthonormal basis that describes the location and orientation of a Dubins vehicle on a sphere (see Fig. 1 of [18]). Furthermore, s represents the arc length traversed by the Dubins vehicle and u_g denotes the geodesic curvature.

We first derive the spherical RS model. When considering an RS path, a new control variable $v \in \{-1, 1\}$ for the velocity needs to be introduced to describe the forward/backward movement of an RS vehicle. To distinguish between the forward/backward movements along the spherical curve $\mathbf{X}(s)$, we define a new set of state vectors, $\mathbf{X}_v(s), \mathbf{T}_v(s)$ and $\mathbf{N}_v(s)$. Here, $\mathbf{X}_v(s) = \mathbf{X}(s)$ represents the position of the RS vehicle on a sphere, $\mathbf{T}_v(s) = v(s)\mathbf{T}(s)$ represents the direction that the RS vehicle is facing, and $\mathbf{N}_v(s) = \mathbf{X}_v(s) \wedge \mathbf{T}_v(s) = v(s)\mathbf{N}(s)$. The relation between $[\mathbf{X}_v(s), \mathbf{T}_v(s), \mathbf{N}_v(s)]$ and $[\mathbf{X}(s), \mathbf{T}(s), \mathbf{N}(s)]$ is shown in Fig. 6. Noting that for the RS model, $v \in \{-1, 1\}$ is piecewise constant and $\frac{ds}{dt} = |v| = 1$,

the new state equations re-parameterized with respect to time⁴ almost everywhere are obtained as $\frac{d\mathbf{X}_v}{dt} = \frac{d\mathbf{X}}{dt} = \mathbf{T}(t) = \mathbf{T}_v(t)/v(t) = v(t)\mathbf{T}_v(t)$, $\frac{d\mathbf{T}_v}{dt} = v(t)\frac{d\mathbf{T}}{dt} = -v(t)\mathbf{X}(t) + v(t)u_g(t)\mathbf{N}(t) = -v(t)\mathbf{X}_v(t) + u_g(t)\mathbf{N}_v(t)$, and $\frac{d\mathbf{N}_v}{dt} = v(t)\frac{d\mathbf{N}}{dt} = -v(t)u_g(t)\mathbf{T}(t) = -u_g(t)\mathbf{T}_v(t)$.

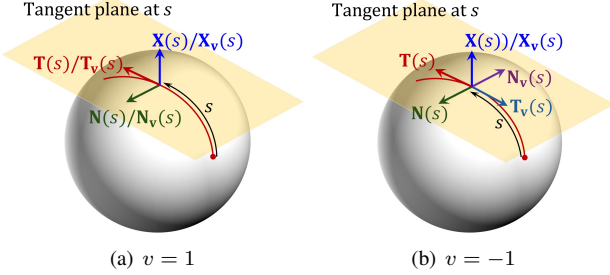


Fig. 6. Relation between $[\mathbf{X}_v(s), \mathbf{T}_v(s), \mathbf{N}_v(s)]$ and $[\mathbf{X}(s), \mathbf{T}(s), \mathbf{N}(s)]$

Analogous to [8], we derive the CRS model by expanding the admissible set of v to $[-1, 1]$, resulting in the formal formulation of the time-optimal spherical CRS problem:

$$J = \min \int_0^T 1 dt \quad (2)$$

subject to

$$\frac{d\mathbf{X}_v}{dt} = v(t)\mathbf{T}_v(t), \quad (3)$$

$$\frac{d\mathbf{T}_v}{dt} = -v(t)\mathbf{X}_v(t) + u_g(t)\mathbf{N}_v(t), \quad (4)$$

$$\frac{d\mathbf{N}_v}{dt} = -u_g(t)\mathbf{T}_v(t), \quad (5)$$

$$\mathbf{R}(0) = \mathbf{I}_3, \quad \mathbf{R}(T) = \mathbf{R}_f, \quad (6)$$

where $v \in [-1, 1]$ and $u_g \in [-U_{max}, U_{max}]$, $\mathbf{R}(t) = [\mathbf{X}_v(t), \mathbf{T}_v(t), \mathbf{N}_v(t)] \in SO(3)$, \mathbf{I}_3 is the identity matrix, and \mathbf{R}_f represents the desired terminal configuration.

Remark 1. In the above model, u_g no longer represents the geodesic curvature. This formulation is analogous to the model in [8] for a CRS vehicle in a plane, where u_g specifies the turning rate and allows for turn-in-place motions when $v = 0$.

For constant v and u_g , the second derivative of $\mathbf{T}_v(t)$ is:

$$\frac{d^2\mathbf{T}_v}{dt^2} = -(v^2(t) + u_g^2(t))\mathbf{T}_v(t), \quad (7)$$

which can be seen as a spring-mass system. When $v = V$ and $u_g = U$ are constants, the solution of (7) is a periodic function $\mathbf{T}_v(t) = \mathbf{T}_v(0) \sin(\omega t - \phi)$ with angular frequency $\omega = \sqrt{V^2 + U^2}$. Hence, from (3), $\mathbf{X}_v(t) = \mathbf{X}_v(0) - \frac{V\mathbf{T}_v(0)}{\omega} \cos(\omega t - \phi)$ is also periodic with angular frequency ω . When $|v| = 1$, the radius of the periodic motion equals $\frac{|v|}{\omega} = \frac{|v|}{\sqrt{V^2 + U^2}} = \frac{1}{\sqrt{1 + U^2}}$, therefore, $|u_g| = U_{max}$ corresponds to a tight turn with radius $r = \frac{1}{\sqrt{1 + U_{max}^2}}$, and $u_g = 0$ corresponds to a great circular arc with radius 1. When $v = 0$ and $|u_g| = U_{max}$, it represents a turn-in-place motion with a turning rate of $\sqrt{0 + U_{max}^2} = U_{max}$.

⁴For Dubins and RS vehicles, time and arc length are equivalent since $|v| = 1$. In contrast, $|v|$ varies for a CRS vehicle, necessitating a re-parameterization.

Note that the state equations, (3)-(5), are equivalent to

$$\frac{d\mathbf{R}(t)}{dt} = \mathbf{R}(t) \underbrace{\begin{pmatrix} 0 & -v(t) & 0 \\ v(t) & 0 & -u_g(t) \\ 0 & u_g(t) & 0 \end{pmatrix}}_{\Omega(t)}. \quad (8)$$

Remark 2. For a satellite with two reaction wheels, following [24] and neglecting its initial angular momentum [25], the satellite's kinematics is obtained as:

$$J\omega_s = e_1 v_1 + e_3 v_2, \quad (9)$$

where $J = \text{diag}(J_1, J_2, J_3)$ denotes the inertia matrix, ω_s denotes the angular velocity vector of the satellite relative to its body frame, $e_1 = [1, 0, 0]^T$, $e_3 = [0, 0, 1]^T$, and $v_i \in [-v_{i,max}, v_{i,max}]$ represent the scaled reaction wheel velocities. Using the above equation and mapping the angular velocity vector to its corresponding skew-symmetric matrix:

$$\frac{d\mathbf{R}(t)}{dt} = \mathbf{R}(t) \begin{pmatrix} 0 & -\frac{v_2(t)}{J_3} & 0 \\ \frac{v_2(t)}{J_3} & 0 & -\frac{v_1(t)}{J_1} \\ 0 & \frac{v_1(t)}{J_1} & 0 \end{pmatrix}, \quad (10)$$

where in this case, $\mathbf{R}(t) \in SO(3)$ represents the pose of the satellite. Redefining new control variables $u_g = \frac{v_1 J_3}{v_{2,max} J_1}$, $v = \frac{v_2}{v_{2,max}}$, and scaling time with $\tau = \frac{v_{2,max}}{J_3} t$, it is obtained that

$$\frac{d\mathbf{R}(\tau)}{d\tau} = \mathbf{R}(\tau)\Omega(\tau), \quad (11)$$

and $v \in [-1, 1]$, $u_g \in [-\frac{v_{1,max} J_3}{v_{2,max} J_1}, \frac{v_{1,max} J_3}{v_{2,max} J_1}]$. It is clear that (8) and (11) are equivalent.

Remark 3. For a spherical rolling robot, following [29], the kinematics describing the robot's pose is as follows:

$$\begin{cases} \dot{x} = \frac{u_1}{R} \frac{\sin(z - \theta_v)}{\cos y} \\ \dot{y} = \frac{u_1}{R} \cos(z - \theta_v) \\ \dot{z} = \frac{u_1}{R} \tan y \sin(z - \theta_v). \end{cases} \quad (12)$$

where x, y , and z denote the Euler angles of the spherical shell relative to a ground-fixed inertial frame, according to the ZYX (or Tait-Bryan) convention. u_1 and θ_v represent the velocity and heading angle of the IDU related to the ground-fixed inertial frame, respectively. Also, $\dot{\theta}_v = u_2$, with u_2 indicating the IDU's yaw rate. R denotes the spherical shell's radius.

Following [29], we assume the projection of geometrical center of the IDU on the ground is always coincident with the contact point of the robot with the ground. To describe the pose kinematics of the shell relative to the IDU, we define a new variable $\bar{z} = z - \theta_v$. It can be observed that x, y , and \bar{z} represent the ZYX Euler angles of the shell relative to a body frame attached to the IDU. By scaling u_1 with $v = \frac{u_1}{R}$ and defining $u_g = -u_2$, it is obtained that

$$\begin{cases} \dot{x} = v \frac{\sin(\bar{z})}{\cos y} \\ \dot{y} = v \cos(\bar{z}) \\ \dot{\bar{z}} = v \tan y \sin(\bar{z}) + u_g. \end{cases} \quad (13)$$

Referring to [35], the above equation is equivalent to the model of a vehicle traveling on a unit sphere using geographic

coordinates, and its equivalence to the model in $SO(3)$ is shown in [35] as well.

Equation (8) can be rewritten in terms of left-invariant vector-fields $\vec{l}_1(\mathbf{R}(t))$ and $\vec{L}_{12}(\mathbf{R}(t))$, defined as

$$\vec{l}_1(\mathbf{R}(t)) = \mathbf{R}(t)l_1 = \mathbf{R}(t) \begin{pmatrix} 0 & -1 & 0 \\ 1 & 0 & 0 \\ 0 & 0 & 0 \end{pmatrix}, \quad (14)$$

$$\vec{L}_{12}(\mathbf{R}(t)) = \mathbf{R}(t)L_{12} = \mathbf{R}(t) \begin{pmatrix} 0 & 0 & 0 \\ 0 & 0 & 1 \\ 0 & -1 & 0 \end{pmatrix}. \quad (15)$$

Here, l_1 and L_{12} lie in $so(3)$, the Lie-algebra of the Lie group $SO(3)$. Equation (8) can therefore be rewritten as

$$\frac{d\mathbf{R}(t)}{dt} = v(t)\vec{l}_1(\mathbf{R}(t)) - u_g(t)\vec{L}_{12}(\mathbf{R}(t)). \quad (16)$$

Similar to [11], PMP is applied for the symplectic formalism [36]. Hence, the Hamiltonian is given by

$$\begin{aligned} H_{u_g(t),v(t)}(\zeta_0, \zeta) &= \zeta_0(1) + \zeta \left(v(t)\vec{l}_1(\mathbf{R}(t)) - u_g(t)\vec{L}_{12}(\mathbf{R}(t)) \right) \\ &= \zeta_0 + v(t)\zeta \left(\vec{l}_1(\mathbf{R}(t)) \right) - u_g(t)\zeta \left(\vec{L}_{12}(\mathbf{R}(t)) \right) \\ &= \zeta_0 + v(t)h_1(\zeta(t)) - u_g(t)H_{12}(\zeta(t)), \end{aligned} \quad (17)$$

where h_1 and H_{12} are smooth functions in $T^*SO(3)$, the cotangent bundle of the Lie group $SO(3)$, and $\zeta \in T^*SO(3)$ is a dual vector for every t .

The Pontryagin maximum principle (PMP) [11], [37]: If $(\mathbf{R}(t), v(t), u_g(t))$ is an optimal trajectory for the system in (8) on an interval $[0, \bar{t}]$, then it is the projection of the integral curve $\zeta(t)$ corresponding to the Hamiltonian vector field associated with the left-invariant vector field using which the system evolves, so that

- 1) $\zeta_0 \leq 0$ and is constant in t .
- 2) If $\zeta_0 = 0$, then $\zeta(t)$ is not identically zero in $[0, \bar{t}]$.
- 3) $H_{u_g(t),v(t)}(\zeta_0, \zeta(t)) \geq H_{\bar{u}_g, \bar{v}}(\zeta_0, \zeta(t))$ for all $\bar{v} \in [-1, 1]$, $\bar{u}_g \in [-U_{max}, U_{max}]$, and almost all $t \in [0, \bar{t}]$.
- 4) $H_{u_g(t),v(t)}(\zeta_0, \zeta(t))$ is zero for almost all $t \in [0, \bar{t}]$.

Furthermore, h_1, h_2 , and H_{12} are Hamiltonians corresponding to the left-invariant vector fields \vec{l}_1, \vec{l}_2 , and \vec{L}_{12} (page 363 of [36]), the Poisson bracket of the Hamiltonians satisfies the same relations as the Lie bracket of the vector fields. That is,

$$[L_{12}, l_1] = l_2, \quad \implies \{H_{12}, h_1\} = h_2, \quad (18)$$

$$[l_1, l_2] = L_{12}, \quad \implies \{h_1, h_2\} = H_{12}, \quad (19)$$

$$[l_2, L_{12}] = l_1, \quad \implies \{h_2, H_{12}\} = h_1. \quad (20)$$

The evolution of the Hamiltonians from PMP are given by⁵ [11]

$$\begin{aligned} \frac{dh_1(\zeta(t))}{dt} &= \{h_1, H_{u_g, v}\} = \{h_1, vh_1 - u_g H_{12}\} \\ &= u_g h_2, \end{aligned} \quad (21)$$

⁵Note that the Poisson bracket with a constant (in this case, ζ_0), is zero.

$$\begin{aligned} \frac{dh_2(\zeta(t))}{dt} &= \{h_2, H_{u_g, v}\} = \{h_2, vh_1 - u_g H_{12}\} \\ &= v\{h_2, h_1\} - u_g\{h_2, H_{12}\} \\ &= -vH_{12} - u_g h_1, \end{aligned} \quad (22)$$

$$\begin{aligned} \frac{dH_{12}(\zeta(t))}{dt} &= \{H_{12}, H_{u_g, v}\} = \{H_{12}, vh_1 - u_g H_{12}\} \\ &= v\{H_{12}, h_1\} = v h_2. \end{aligned} \quad (23)$$

Noting that $\zeta_0 = 0$ corresponds to the abnormal case, we have the following lemma:

Lemma 1. *No nontrivial abnormal extremal path exists.*

Proof. By Condition 4) of PMP, $H_{u_g, v} \equiv 0$. Condition 3) of PMP implies that $vh_1 \geq 0$, $u_g H_{12} \leq 0$, $u_g \neq 0$ if $H_{12} \neq 0$, and $v \neq 0$ if $h_1 \neq 0$. If $\zeta_0 = 0$, then $H_{u_g, v} = vh_1 - u_g H_{12} \equiv 0$, which is only possible when $h_1 \equiv 0$ and $H_{12} \equiv 0$. Furthermore, by (21) and (23), $\frac{dH_{12}}{dt} = v h_2 \equiv 0$ and $\frac{dh_1}{dt} = u_g h_2 \equiv 0$, which indicate either $h_2 \equiv 0$ or $v = u_g \equiv 0$. The latter case results in $\frac{d\mathbf{R}(t)}{dt} \equiv 0$ from (8), hence, it corresponds to a non-moving path, which is trivially non-optimal for a minimum-time problem. The former case results in $h_1 = h_2 = H_{12} \equiv 0$ and violates condition 2) of PMP [11]. \square

Remark 4. *Since $\zeta_0 \leq 0$, and $\zeta_0 \neq 0$ by Lemma 1, hence, $\zeta_0 < 0$. Furthermore, $\zeta_0 < 0$ can be normalized to $\zeta_0 = -1$ without loss of generality [11]. Therefore, hereafter, for a nontrivial extremal path, we treat ζ_0 as -1 .*

Thus far, the Hamiltonian can be further simplified with Remark 4. Furthermore, for the simplicity of symbols and the uniformity of signs of the control variables, we define:

$$\mathcal{A} := H_{12}, \quad \mathcal{B} := h_2, \quad \mathcal{C} := -h_1, \quad (24)$$

accordingly,

$$\frac{d\mathcal{A}}{dt} = v\mathcal{B}, \quad \frac{d\mathcal{B}}{dt} = -v\mathcal{A} + u_g\mathcal{C}, \quad \frac{d\mathcal{C}}{dt} = -u_g\mathcal{B}. \quad (25)$$

Therefore, the Hamiltonian in (17) simplifies to:

$$H_{u_g, v} = -1 - v\mathcal{C} - u_g\mathcal{A}, \quad (26)$$

From PMP, v and u_g pointwise maximize $H_{u_g, v}$, therefore:

$$v = \begin{cases} -1 & \text{if } \mathcal{C} > 0 \\ 1 & \text{if } \mathcal{C} < 0 \end{cases}, \quad u_g = \begin{cases} -U_{max} & \text{if } \mathcal{A} > 0 \\ U_{max} & \text{if } \mathcal{A} < 0 \end{cases}. \quad (27)$$

By (27), it is clear that v and u_g switch between extreme values when \mathcal{C} and \mathcal{A} change sign, respectively. Next, we analyze the cases where $\mathcal{C} = 0$ or $\mathcal{A} = 0$.

Lemma 2. *On a nontrivial extremal path, $|\mathcal{C}| = 1$ if $\mathcal{A} = 0$, $|\mathcal{A}| = \frac{1}{U_{max}}$ if $\mathcal{C} = 0$, $u_g \equiv 0$ iff $\mathcal{A} \equiv 0$, and $v \equiv 0$ iff $\mathcal{C} \equiv 0$.*

Proof. By Condition 4) of PMP, (26), and (27), $-1 + |\mathcal{C}| = 0$ if $\mathcal{A} = 0$ and $-1 + U_{max}|\mathcal{A}| = 0$ if $\mathcal{C} = 0$. Hence, $|\mathcal{C}| = 1$ if $\mathcal{A} = 0$ and $|\mathcal{A}| = \frac{1}{U_{max}}$ if $\mathcal{C} = 0$.

If $\mathcal{A} = 0$, then $|\mathcal{C}| \equiv 1$. Furthermore, by (25), $\frac{d\mathcal{A}}{dt} = v\mathcal{B} \equiv 0$, which implies $\mathcal{B} \equiv 0$ since $v \neq 0$. Hence, $\frac{d\mathcal{B}}{dt} = -v\mathcal{A} + u_g\mathcal{C} \equiv 0$. Therefore, $u_g \equiv 0$. On the contrary, if $u_g \equiv 0$, then $\mathcal{A} \equiv 0$ since by (27), $u_g \neq 0$ if $\mathcal{A} \neq 0$. Hence, $u_g \equiv 0$ iff $\mathcal{A} \equiv 0$.

Similarly, if $\mathcal{C} \equiv 0$, then $|\mathcal{A}| \equiv \frac{1}{U_{max}}$, and $u_g \neq 0$ by (27). Furthermore, $\frac{d\mathcal{C}}{dt} = -u_g \mathcal{B} \equiv 0$, which implies $\mathcal{B} \equiv 0$. Hence, $\frac{d\mathcal{B}}{dt} = -v\mathcal{A} + u_g \mathcal{C} \equiv 0$, which implies that $v \equiv 0$. On the contrary, if $v \equiv 0$, then $\mathcal{C} \equiv 0$ since by (27), $v \neq 0$ if $\mathcal{C} \neq 0$. Hence, $v \equiv 0$ iff $\mathcal{C} \equiv 0$. \square

Therefore, the optimal control actions are given by

$$v = \begin{cases} -1 & \text{if } \mathcal{C} > 0 \\ 0 & \text{if } \mathcal{C} = 0 \\ 1 & \text{if } \mathcal{C} < 0 \end{cases}, \quad u_g = \begin{cases} -U_{max} & \text{if } \mathcal{A} > 0 \\ 0 & \text{if } \mathcal{A} = 0 \\ U_{max} & \text{if } \mathcal{A} < 0 \end{cases}. \quad (28)$$

Throughout this paper, we will denote a segment that is an arc of a great circle (with $u_g = 0, v = \pm 1$) as “G”, a turn-in-place motion (with $u_g = \pm 1, v = 0$) as “T”, and a segment that is a tight turn (with $u_g = \pm 1, v = \pm 1$) as “C”. A cusp, which corresponds to a change in the value of v between 1 and -1 , will be denoted as “|”. Fig. 7 illustrates a cusp on a C|C path. For instance, “GC|CT” represents a path starting as a segment of a great circle arc, followed by two tight turns joined by a cusp, and concluding with a turn-in-place motion.

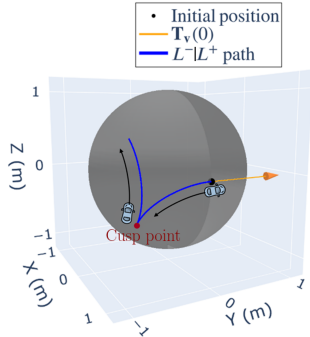


Fig. 7. Cusp on a C|C path

If specific actions need to be declared, we will use “L” and “R” to denote $u_g = U_{max}$ and $u_g = -U_{max}$, respectively, and superscripts “+”, “0”, and “-” to represent $v = 1, v = 0$ and $v = -1$, respectively. All possible segment types are visualized in Fig. 8. Furthermore, we will use subscripts to denote the arc angle of a segment when they need to be specified. For instance, “ $L^+_\alpha G^+_\beta R^-_\gamma R^0_\sigma$ ” represents a path that is a concatenation of a tight turn segment (with $u_g = U_{max}, v = 1$) with an angle of α ; an arc segment of a great circle (with $u_g = 0, v = 1$) with an angle of β ; a tight turn segment (with $u_g = -U_{max}, v = -1$) with an angle of γ ; and a segment of a turn-in-place motion (with $u_g = -U_{max}, v = 0$) with an angle of σ .

III. BRIEF ANALYSIS OF THE OPTIMAL PATHS

In this section, we present the phase portrait of \mathcal{A} and \mathcal{C} and give some brief results on the optimal paths. Furthermore, we show that the problem of characterizing optimal path types can be divided into three cases.

Since the control actions v and u_g depend on \mathcal{C} and \mathcal{A} , respectively, the optimal path can be characterized by the evolution of \mathcal{C} and \mathcal{A} . By (26) and further with $H_{u_g, v} \equiv 0$, a clear \mathcal{A} - \mathcal{C} relation is obtained:

$$1 + v\mathcal{C} + u_g\mathcal{A} \equiv 0. \quad (29)$$

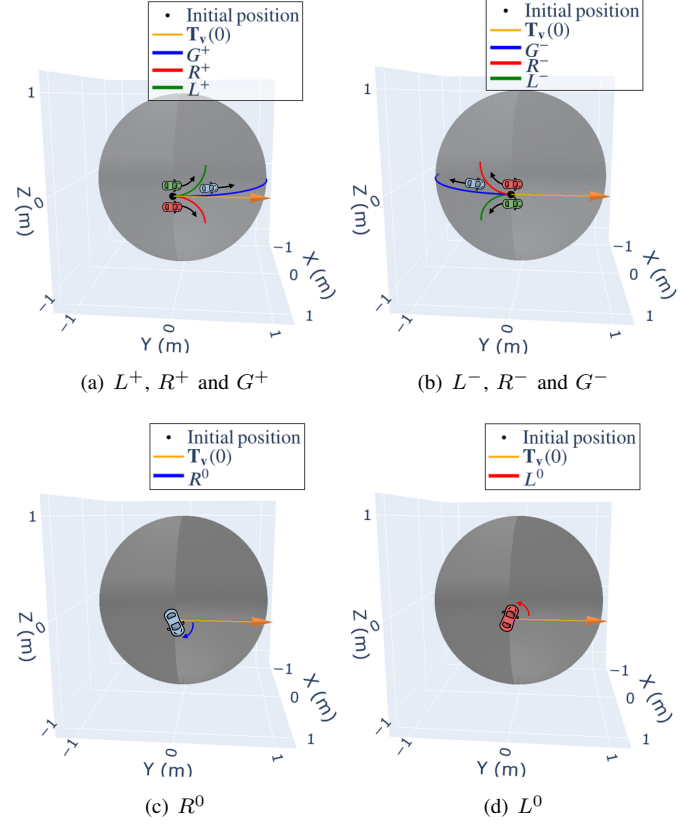


Fig. 8. Possible segment types on an extremal path

Further supplemented by (28), the shape of the \mathcal{A} - \mathcal{C} phase portrait is visualized in Fig. 9, with the evolution directions of \mathcal{A} and \mathcal{C} to be analyzed.

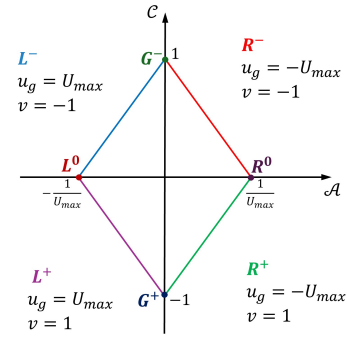


Fig. 9. Phase portrait of \mathcal{A} - \mathcal{C}

Remark 5. (a) By Lemma 2 and equation (29) (shown in Fig. 9), \mathcal{A} and \mathcal{C} cannot have any common zero, therefore u_g and v cannot switch value at the same time instance. Since “|” represents a cusp, a “CC” path can only represent two segments joined by an inflection point, corresponding to a change of the value of u_g between U_{max} and $-U_{max}$.

(b) By (28), the points $(-\frac{1}{U_{max}}, 0)$ and $(\frac{1}{U_{max}}, 0)$ in the phase portrait correspond to either cusps or T segments, and $(0, -1)$ and $(0, 1)$ correspond to either inflection points or G segments.

Lemma 3. A path evolves clockwise in the $\mathcal{A} - \mathcal{C}$ portrait if $\mathcal{B} < 0$, and counter-clockwise if $\mathcal{B} > 0$.

Proof. Suppose $\mathcal{B} < 0$. Since $u_g = -U_{max}$ within the right half plane of Fig. 9, by (25), $\frac{d\mathcal{C}}{dt} = -u_g\mathcal{B} < 0$ within the right half plane. Similarly, it can be obtained that $\frac{d\mathcal{C}}{dt} > 0$ within the left half plane. At point $(0, 1)$, since $v = -1$, by (25), $\frac{d\mathcal{A}}{dt} = v\mathcal{B} > 0$. Similarly, it can be obtained that $\frac{d\mathcal{A}}{dt} < 0$ at $(0, -1)$. Therefore, the path evolves clockwise.

With a similar proof for $\mathcal{B} > 0$, the lemma is proved. \square

We now derive some results that will be useful throughout the upcoming sections.

Note that $\frac{d\mathcal{A}}{dt} = v\mathcal{B}$, \mathcal{B} is differentiable, and v remains constant within each of the quadrants of the phase portrait, hence, $\frac{d\mathcal{A}}{dt}$ is differentiable within each quadrant. By (25),

$$\frac{d^2\mathcal{A}}{dt^2} = v \frac{d\mathcal{B}}{dt} = -v^2\mathcal{A} + u_g v\mathcal{C}. \quad (30)$$

Furthermore, substituting for $v\mathcal{C}$ from (29), we get

$$\frac{d^2\mathcal{A}}{dt^2} = -(v^2 + u_g^2)\mathcal{A} - u_g. \quad (31)$$

By (28), if $\mathcal{A} \neq 0$ and $\mathcal{C} \neq 0$, then $v^2 = 1$ and $u_g^2 = U_{max}^2$. Hence, within each quadrant, we have the solution of $\mathcal{A}(t)$ and $\frac{d\mathcal{A}(t)}{dt}$ as follows:

$$\mathcal{A}(t) = \lambda_{\mathcal{A}} \sin(\sqrt{1 + U_{max}^2}t - \phi_{\mathcal{A}}) - \frac{u_g}{1 + U_{max}^2}, \quad (32)$$

$$\frac{d\mathcal{A}(t)}{dt} = \lambda_{\mathcal{A}} \sqrt{1 + U_{max}^2} \cos(\sqrt{1 + U_{max}^2}t - \phi_{\mathcal{A}}), \quad (33)$$

where $\lambda_{\mathcal{A}} \geq 0$. Similarly,

$$\mathcal{C}(t) = \lambda_{\mathcal{C}} \sin(\sqrt{1 + U_{max}^2}t - \phi_{\mathcal{C}}) - \frac{v}{1 + U_{max}^2}, \quad (34)$$

$$\frac{d\mathcal{C}(t)}{dt} = \lambda_{\mathcal{C}} \sqrt{1 + U_{max}^2} \cos(\sqrt{1 + U_{max}^2}t - \phi_{\mathcal{C}}), \quad (35)$$

where $\lambda_{\mathcal{C}} \geq 0$.

It is also worth noting that, by (25), $\frac{d(\mathcal{A}^2(t) + \mathcal{B}^2(t) + \mathcal{C}^2(t))}{dt} = 2(\mathcal{A}(t)\frac{d\mathcal{A}(t)}{dt} + \mathcal{B}(t)\frac{d\mathcal{B}(t)}{dt} + \mathcal{C}(t)\frac{d\mathcal{C}(t)}{dt}) \equiv 0$. Therefore,

$$\mathcal{A}^2(t) + \mathcal{B}^2(t) + \mathcal{C}^2(t) \equiv g, \quad (36)$$

where g is a non-negative constant over a trajectory.

From (29), $|\mathcal{C}| = 1 - U_{max}|\mathcal{A}|$, hence, from (36), $\mathcal{B}^2(t) = g - 1 - \mathcal{A}^2(t) - U_{max}\mathcal{A}^2(t) + 2U_{max}|\mathcal{A}(t)|$. Three cases arise for obtaining the sufficient list of optimal path types: (1) $g = 1$; (2) $g > 1$; (3) $g < 1$. These three cases will be analyzed in detail in Sections IV, V, and VI, respectively. We provide an overview of the connections between the upcoming lemmas, corollaries, and propositions with Theorem 1, in Fig. 10, along with summaries of the key results.

We outline the proof of the main result for the case $g = 1$ by explicitly listing below the key results on which it is built; the proofs of these results will follow in detail in the following section.

Remark 6. Throughout this paper, we define the angle $\beta = \arctan\left(\frac{1}{\sqrt{U_{max}^4 - 1}}\right) + \frac{\pi}{2}$, which will be utilized extensively.

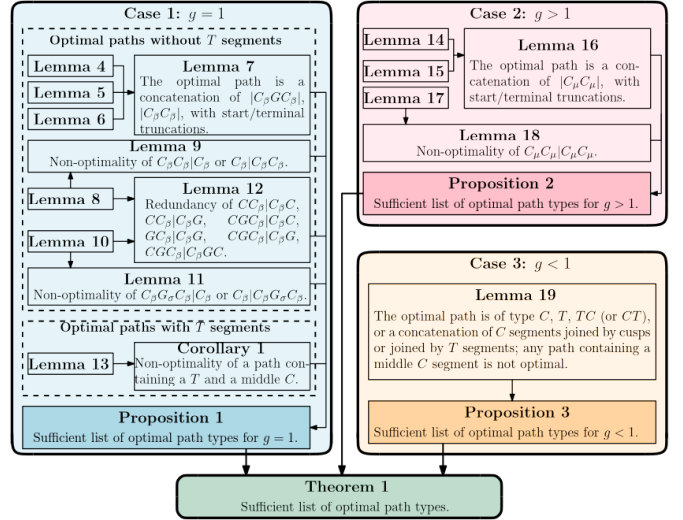


Fig. 10. Connections between proofs

Remark 7. The starting and terminal segments of any candidate optimal path with at least $n \geq 3$ segments will sometimes be referred to as boundary segments, and the other $n - 2$ segments will be referred to as middle segments. For example, in the path $CC_\beta|C$, the middle segment is C_β and in $C|C_\beta GC_\beta|C$, the middle segments are C_β, G .

Lemma 7. For $g = 1$ and $U_{max} \geq 1$ (or $r \leq \frac{1}{\sqrt{2}}$), an optimal path without T segments is a concatenation of $|C_\beta GC_\beta|$ and $|C_\beta C_\beta|$ sub-paths, where the start/terminal sub-paths can be truncated⁶.

Lemma 9. A $C_\beta C_\beta | C_\beta$ (or $C_\beta | C_\beta C_\beta$) path is not optimal.

Lemma 11. For $\sigma \geq 0$, a path of type $C_\beta G_\sigma C_\beta | C_\beta$ (or $C_\beta | C_\beta G_\sigma C_\beta$) is not optimal.

Lemma 12. Paths of type $CC_\beta | C_\beta C$, $CC_\beta | C_\beta G$, $CGC_\beta | C_\beta C$, $GC_\beta | C_\beta G$, $CGC_\beta | C_\beta G$, and $CGC_\beta | C_\beta GC$ are redundant⁷. They may be replaced respectively by paths of type $C|C$, $C|C_\beta G$, $CGC_\beta | C$, $C|C_\beta G$, $C|C_\beta G$, and $CGC_\beta | C$.

Corollary 1. For $g = 1$ and $U_{max} \geq 1$ (or $r \leq \frac{1}{\sqrt{2}}$), a path containing a T segment and a middle C segment is not optimal.

Given these key results, we now prove how the main result for $g = 1$, stated in Proposition 1, can be obtained.

Proposition 1. For $g = 1$ and $U_{max} \geq 1$ (or $r \leq \frac{1}{\sqrt{2}}$), the optimal path may be restricted to the following types, together with their symmetric forms⁸:

$$\begin{aligned} & C, G, T, CC, GC, C|C, TC, \\ & CC_\beta | C, CGC, C|C_\beta G, CTC, \\ & C|C_\beta C_\beta | C, CGC_\beta | C, C|C_\beta GC_\beta | C, \\ & \text{where } \beta = \arctan\left(\frac{1}{\sqrt{U_{max}^4 - 1}}\right) + \frac{\pi}{2}. \end{aligned}$$

⁶The start sub-paths may be truncated to $CGC_\beta|$, $GC_\beta|$, $C_\beta|$, or $CC_\beta|$, and the terminal sub-paths may be truncated to $|C_\beta GC$, $|C_\beta G$, $|C_\beta$, or $|C_\beta C$.

⁷If a path is redundant, it means that there is always an alternative path of same cost, belonging to the sufficient list, with fewer segments.

⁸By the term ‘‘symmetric form’’, we mean the reversal of a string, for example, the symmetric form of the path type $C|C_\beta G$ is $GC_\beta | C$.

Proof. The list in Proposition 1 can be categorized into two mutually disjoint sets: (1) paths without T segments, and (2) paths containing at least one T segment.

For set (1), notice that Lemma 7 dictates that the optimal paths can only be a concatenation of $|C_\beta GC_\beta|$ and $|C_\beta C_\beta|$ with the start and terminal sub-paths, say P_i and P_f , potentially being truncated. Lemmas 9 and 11 rule out the optimality of paths containing two or more contiguous middle sub-paths of the form $|C_\beta GC_\beta|$ and $|C_\beta C_\beta|$; hence, it is sufficient to consider paths with one or no middle sub-path. Paths with one middle sub-path are of the forms (a) $P_i|C_\beta GC_\beta|P_f$ and (b) $P_i|C_\beta C_\beta|P_f$, where $P_i \in \{C, GC_\beta, CC_\beta, CGC_\beta\}$ and $P_f \in \{C, C_\beta G, C_\beta C, C_\beta GC\}$. Notice that, if $P_i \in \{GC_\beta, CC_\beta, CGC_\beta\}$ or $P_f \in \{C_\beta G, C_\beta C, C_\beta GC\}$, forms (a) and (b) contain $C_\beta G_\sigma C_\beta|C_\beta$ (or $C_\beta|C_\beta G_\sigma C_\beta$) and $C_\beta C_\beta|C_\beta$ (or $C_\beta|C_\beta C_\beta$), respectively. Therefore, their non-optimality follows from Lemma 11 and Lemma 9, respectively. If $P_i = P_f = C$, forms (a) and (b) become $C|C_\beta GC_\beta|C$ and $C|C_\beta C_\beta|C$, respectively, and belong to the sufficient list. This leaves us with the paths $C|C_\beta GC_\beta|C$, $C|C_\beta C_\beta|C$, and paths in the forms $P_i|P_f$ and P_s in set (1), where $P_i \in \{C, GC_\beta, CC_\beta, CGC_\beta\}$, $P_f \in \{C, C_\beta G, C_\beta C, C_\beta GC\}$, and $P_s \in \{C, G, GC, CG, CC, CGC\}$. By Lemma 12, the instances of $P_i|P_f$ of types $CC_\beta|C_\beta G$, $CGC_\beta|C_\beta C$, $GC_\beta|C_\beta G$, $CGC_\beta|C_\beta G$, and $CGC_\beta|C_\beta GC$ (and their symmetric forms) are redundant. With these types removed, set (1) is only left with the path types without T segments listed in Proposition 1.

For set (2), from the phase portrait in Fig. 9, since $\mathcal{A}(t)$ and $\mathcal{C}(t)$ are continuous, a L^0 (or R^0) segment can only be preceded and followed by a L (or R) segment. Therefore, an optimal path containing T segments is of the form $P_l TP_r$, where P_l is either empty or ends with a C segment, and P_r is either empty or starts with a C segment. Furthermore, it can be concluded that P_l and P_r are both at most a C segment. Otherwise, the $P_l TP_r$ path contains a middle C segment and is non-optimal by Corollary 1. Hence, set (2) consists of the path types T , TC , CT , CTC . \square

IV. OPTIMAL PATHS FOR $g = 1$

This section offers the detailed proofs of the key results for $g = 1$, including Lemmas 7, 9, 11, 12, and Corollary 1, which are utilized for Proposition 1, together with their supporting lemmas illustrated in Fig. 10.

Notice that $\tan^{-1}(\frac{y}{x})$ is not defined at $y = \pm 1$ & $x = 0$. In this article, we define $\arctan(\cdot)$ as

$$\arctan\left(\frac{y}{x}\right) = \begin{cases} \frac{\pi}{2} & \text{if } y = 1 \text{ \& } x = 0 \\ -\frac{\pi}{2} & \text{if } y = -1 \text{ \& } x = 0 \\ \tan^{-1}\left(\frac{y}{x}\right) & \text{otherwise} \end{cases} \quad (37)$$

The following Lemmas 4-6 will be useful throughout this section.

Lemma 4. *For $g = 1$, the angle of a C segment that is completely traversed⁹ clockwise/counter-clockwise is exactly $\arctan\left(\frac{1}{\sqrt{U_{max}^4 - 1}}\right) + \frac{\pi}{2}$ radians.*

⁹A C segment is completely traversed if $|C|$ monotonically increases from 0 to 1 or monotonically decreases from 1 to 0 along the C segment.

Proof. Consider a R^- segment that is completely traversed clockwise in the phase portrait. Let t_1 denote the time spent on the R^- segment. From Fig. 9, on the R^- segment, $\mathcal{A}(0) = 0$, $\mathcal{C}(0) = 1$, $\mathcal{A}(t_1) = \frac{1}{U_{max}}$, and $\mathcal{C}(t_1) = 0$. By (36), $\mathcal{B}(0) = \pm\sqrt{g-1}$ and $\mathcal{B}(t_1) = \pm\sqrt{g - \frac{1}{U_{max}^2}}$. Since the segment is traversed clockwise, $\frac{d\mathcal{C}}{dt} < 0$ from Fig. 9. Furthermore, since $u_g = -U_{max}$ on a R^- segment, $\mathcal{B} < 0$ by (25). Hence, $\mathcal{B}(0) = -\sqrt{g-1}$ and $\mathcal{B}(t_1) = -\sqrt{g - \frac{1}{U_{max}^2}}$. From (25), $\frac{d\mathcal{A}}{dt}(0) = v\mathcal{B}(0) = \sqrt{g-1}$ and $\frac{d\mathcal{A}}{dt}(t_1) = v\mathcal{B}(t_1) = \sqrt{g - \frac{1}{U_{max}^2}}$. Furthermore, from (32) and (33), on the R^- segment,

$$\mathcal{A}(0) = \lambda_A \sin(-\phi_A) + \frac{U_{max}}{1 + U_{max}^2} = 0, \quad (38)$$

$$\frac{d\mathcal{A}}{dt}(0) = \lambda_A \sqrt{1 + U_{max}^2} \cos(-\phi_A) = \sqrt{g-1}, \quad (39)$$

$$\mathcal{A}(t_1) = \lambda_A \sin(\sqrt{1 + U_{max}^2} t_1 - \phi_A) + \frac{U_{max}}{1 + U_{max}^2} = \frac{1}{U_{max}}, \quad (40)$$

$$\begin{aligned} \frac{d\mathcal{A}}{dt}(t_1) &= \lambda_A \sqrt{1 + U_{max}^2} \cos(\sqrt{1 + U_{max}^2} t_1 - \phi_A) \\ &= \sqrt{g - \frac{1}{U_{max}^2}}. \end{aligned} \quad (41)$$

Hence, $\lambda_A \sin(-\phi_A) = -\frac{U_{max}}{1 + U_{max}^2}$, $\lambda_A \cos(-\phi_A) = \frac{\sqrt{g-1}}{\sqrt{1 + U_{max}^2}}$, $\lambda_A \sin(\sqrt{1 + U_{max}^2} t_1 - \phi_A) = \frac{1}{U_{max}(1 + U_{max}^2)}$, $\lambda_A \cos(\sqrt{1 + U_{max}^2} t_1 - \phi_A) = \frac{\sqrt{g - \frac{1}{U_{max}^2}}}{\sqrt{1 + U_{max}^2}}$. Therefore,

$$t_1 = \frac{1}{\sqrt{1 + U_{max}^2}} \left(\arctan\left(\frac{1}{U_{max} \sqrt{(g - \frac{1}{U_{max}^2})(1 + U_{max}^2)}}\right) - \arctan\left(\frac{-U_{max}}{\sqrt{(g-1)(1 + U_{max}^2)}}\right) \right). \quad (42)$$

Let α_1 and ω_1 denote the arc angle and angular frequency of the R^- segment, respectively. Note that $\alpha_1 = \omega_1 t_1$, and $\omega_1 = \sqrt{1 + U_{max}^2}$. Therefore,

$$\begin{aligned} \alpha_1 &= \arctan\left(\frac{1}{U_{max} \sqrt{(g - \frac{1}{U_{max}^2})(1 + U_{max}^2)}}\right) \\ &\quad - \arctan\left(\frac{-U_{max}}{\sqrt{(g-1)(1 + U_{max}^2)}}\right). \end{aligned} \quad (43)$$

When $g = 1$, $\alpha_1 = \arctan\left(\frac{1}{\sqrt{U_{max}^4 - 1}}\right) + \frac{\pi}{2}$.

Using similar results for a R^- segment completely traversed counter-clockwise, and segments R^+ , L^- , and L^+ , the lemma is proved. \square

According to Lemma 3, the sign of \mathcal{B} reveals the evolution direction of an optimal path on the phase portrait. Consequently, in the subsequent lemma, we examine the locations on the phase portrait where \mathcal{B} may reach 0, indicating where an optimal path can switch its evolution direction on the portrait.

Lemma 5. For $g = 1$, $\mathcal{B} = 0$ is possible only at $\mathcal{A} = 0$ for $U_{max} > 1$ (or $r < \frac{1}{\sqrt{2}}$), and at $\mathcal{A} = 0, \pm \frac{1}{U_{max}}$ for $U_{max} = 1$ (or $r = \frac{1}{\sqrt{2}}$).

Proof. Within the left half plane of Fig. 9, (29) becomes $1 - |\mathcal{C}| + U_{max}\mathcal{A} \equiv 0$, hence, $\mathcal{C}^2 = (1 + U_{max}\mathcal{A})^2$, and

$$f(\mathcal{A}) := \mathcal{A}^2 + \mathcal{C}^2 = (1 + U_{max}^2)(\mathcal{A} + \frac{U_{max}}{1 + U_{max}^2})^2 + \frac{1}{1 + U_{max}^2}. \quad (44)$$

$f(\mathcal{A})$ is a quadratic function of \mathcal{A} with a positive leading coefficient and the minimizer located at $\mathcal{A} = -\frac{U_{max}}{1 + U_{max}^2}$. Hence, $\arg \max_{\mathcal{A}} f(\mathcal{A}) = \arg \max_{\mathcal{A}} |\mathcal{A} - (-\frac{U_{max}}{1 + U_{max}^2})|$. Note that within the left half plane, $\mathcal{A} \in [-\frac{1}{U_{max}}, 0]$, it suffices to evaluate the boundary points of \mathcal{A} to obtain $\max_{\mathcal{A}} f(\mathcal{A})$.

In the case of $U_{max} > 1$, $|0 - (-\frac{U_{max}}{1 + U_{max}^2})| = \frac{U_{max}^2}{U_{max} + U_{max}^3} > \frac{1}{U_{max} + U_{max}^3} = |-\frac{1}{U_{max}} - (-\frac{U_{max}}{1 + U_{max}^2})|$. Therefore, $f(\mathcal{A}) = \mathcal{A}^2 + \mathcal{C}^2$ reaches its maximum, 1, at a unique maximizer $\mathcal{A} = 0$. Since $\mathcal{A}^2 + \mathcal{B}^2 + \mathcal{C}^2 \equiv g = 1$, $\mathcal{B} = 0$ is only possible at $\mathcal{A} = 0$ in the left half plane.

In the special case of $U_{max} = 1$, then $|0 - (-\frac{U_{max}}{1 + U_{max}^2})| = \frac{1}{2} = |-\frac{1}{U_{max}} - (-\frac{U_{max}}{1 + U_{max}^2})|$, and $\max_{\mathcal{A}} f(\mathcal{A}) = f(0) = f(-\frac{1}{U_{max}}) = 1$. Since $\mathcal{A}^2 + \mathcal{B}^2 + \mathcal{C}^2 \equiv g = 1$, $\mathcal{B} = 0$ is only possible at $\mathcal{A} = 0$ and $\mathcal{A} = -\frac{1}{U_{max}}$ in the left half plane.

With a similar analysis for the right half plane of Fig. 9, the lemma is proved. \square

Remark 8. By Lemma 3, a path evolves clockwise in the \mathcal{A} - \mathcal{C} portrait if $\mathcal{B} < 0$ and counter-clockwise if $\mathcal{B} > 0$. Since \mathcal{B} is continuous, by Lemma 5, for $g = 1$ and $U_{max} > 1$, a path can only switch its direction of evolution (i.e. clockwise/counter-clockwise) at points $(0, \pm 1)$. Furthermore, at points $(0, \pm 1)$, which correspond to G segments or inflection points, since $\mathcal{B} = 0$, we have $\frac{d\mathcal{A}}{dt} = v\mathcal{B} = 0$ and $\frac{d\mathcal{C}}{dt} = -u_g\mathcal{B} = 0$. Hence, it is possible for a path to stay at these points on the portrait and enter a G segment. Similarly, in the special case of $U_{max} = 1$, it is possible for a path to switch its evolution direction at the points $(0, \pm 1)$ or $(\pm \frac{1}{U_{max}}, 0)$, and enter G or T segments at these points.

Remark 9. Lemma 5 and Remark 8 demonstrate that, for $g = 1$, a T segment can appear in an optimal path solely when $U_{max} = 1$. This observation simplifies the characterization of optimal path types by dividing them into two groups: those lacking T segments and those containing them. This will be elaborated upon later in this section.

Recall the differential equation in (8), since v and u_g remain constant on each segment, its solution on each segment is

$$\mathbf{R}(t) = \mathbf{R}(t_i)e^{(t-t_i)\Omega}, \quad (45)$$

where t_i denotes the initial time of the i^{th} segment. It is simpler to deal with arc angles instead of time; hence, we define $\phi = \omega(t-t_i) = \sqrt{v^2 + u_g^2}(t-t_i)$, where ϕ represents the arc angle, and ω denotes the angular frequency as shown in Section II. Let $\hat{\Omega} = \frac{1}{\sqrt{v^2 + u_g^2}}\Omega$. We define $\mathbf{M}(\phi) := e^{\phi\hat{\Omega}} = e^{(t-t_i)\Omega}$. Substituting specific values of v and u_g , $\mathbf{M}(\phi)$ for each type of

segment can be calculated using the Euler-Rodriguez formula [18]. Hence, we obtain

$$\mathbf{M}_{G^+}(\phi) = \begin{pmatrix} c(\phi) & -s(\phi) & 0 \\ s(\phi) & c(\phi) & 0 \\ 0 & 0 & 1 \end{pmatrix}, \quad (46)$$

$$\mathbf{M}_{L^+}(r, \phi) = \begin{pmatrix} \eta_{11} & -rs(\phi) & \eta_{13} \\ rs(\phi) & c(\phi) & -\eta_{23} \\ \eta_{13} & \eta_{23} & \eta_{33} \end{pmatrix}, \quad (47)$$

$$\mathbf{M}_{R^+}(r, \phi) = \begin{pmatrix} \eta_{11} & -rs(\phi) & -\eta_{13} \\ rs(\phi) & c(\phi) & \eta_{23} \\ -\eta_{13} & -\eta_{23} & \eta_{33} \end{pmatrix}, \quad (48)$$

$$\mathbf{M}_{L^0}(\phi) = \begin{pmatrix} 1 & 0 & 0 \\ 0 & c(\phi) & -s(\phi) \\ 0 & s(\phi) & c(\phi) \end{pmatrix}, \quad (49)$$

$$\mathbf{M}_{G^-}(\phi) = \mathbf{M}_{G^+}^T(\phi), \quad (50)$$

$$\mathbf{M}_{L^-}(r, \phi) = \mathbf{M}_{R^+}^T(r, \phi), \quad (51)$$

$$\mathbf{M}_{R^-}(r, \phi) = \mathbf{M}_{L^+}^T(r, \phi), \quad (52)$$

$$\mathbf{M}_{R^0}(\phi) = \mathbf{M}_{L^0}^T(\phi), \quad (53)$$

where $\eta_{11} = 1 - (1 - c(\phi))r^2$, $\eta_{13} = (1 - c(\phi))r\sqrt{1 - r^2}$, $\eta_{23} = s(\phi)\sqrt{1 - r^2}$, $\eta_{33} = c(\phi) + (1 - c(\phi))r^2$, $c(\phi) = \cos(\phi)$, and $s(\phi) = \sin(\phi)$.

Remark 10. Please note that, when we focus on paths not containing T segments, all such paths adhere to $|v| = 1$, so comparing their lengths is effectively the same as comparing their times.

The subsequent lemma will be employed frequently throughout this paper.

Lemma 6. For $\alpha > 0$, a $C_{\pi+\alpha}$ path is not optimal.

Proof. Consider a $L_{\pi+\alpha}^-$ path, where $\alpha > 0$. If $\alpha \geq \pi$, the path is obviously not optimal, as the initial and terminal configurations coincide for a C path with angle of 2π . Otherwise, if $0 < \alpha < \pi$, it is claimed that there exists an alternate $R_{\pi-\alpha}^+$ path that is shorter. Since $0 < \alpha < \pi$, $\pi - \alpha < \pi + \alpha$, the alternate path is shorter, hence, it suffices to show that $\mathbf{M}_{L^-}(r, \pi + \alpha) = \mathbf{M}_{R^+}(r, \pi - \alpha)$. It can be obtained that $\sin(\pi + \alpha) = -\sin(\alpha)$, $\cos(\pi + \alpha) = -\cos(\alpha)$, $\sin(\pi - \alpha) = \sin(\alpha)$, and $\cos(\pi - \alpha) = -\cos(\alpha)$. Substituting these values into (51) and (48), it is obtained that

$$\begin{aligned} \mathbf{M}_{L^-}(r, \pi + \alpha) &= \mathbf{M}_{R^+}(r, \pi - \alpha) \\ &= \begin{pmatrix} \xi_1 & -rs(\alpha) & \xi_2 \\ rs(\alpha) & -c(\alpha) & \xi_3 \\ \xi_2 & -\xi_3 & \xi_4 \end{pmatrix}, \end{aligned} \quad (54)$$

where $\xi_1 = (-c(\alpha) - 1)r^2 + 1$, $\xi_2 = -r\sqrt{1 - r^2}(c(\alpha) + 1)$, $\xi_3 = s(\alpha)\sqrt{1 - r^2}$, $\xi_4 = (r^2 - 1)(c(\alpha) + 1) + 1$.

The non-optimality of $L_{\pi+\alpha}^-$ is visualized in Fig. 11 for $\alpha = \frac{\pi}{2}$ and $U_{max} = 3$ (or $r = \frac{1}{\sqrt{10}}$).

With similar proofs for path types $L_{\pi+\alpha}^+$, $R_{\pi+\alpha}^+$, and $R_{\pi+\alpha}^-$, the lemma is proved. \square

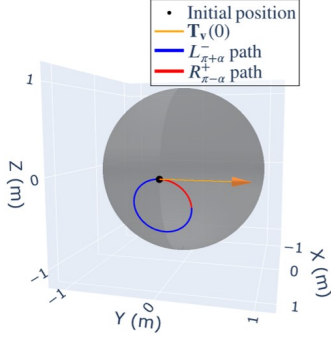


Fig. 11. Non-optimality of $L_{\pi+\alpha}^-$

As noted in Remark 9, when $g = 1$, an optimal path can contain T segments only if $U_{max} = 1$ (or $r = \frac{1}{\sqrt{2}}$). Therefore, we analyze the case where $g = 1$ by distinguishing between paths without T segments and those that contain them.

A. Optimal Paths Without T Segments

To characterize the optimal paths without T segments, we first utilize Lemmas 4-6 to derive the key result Lemma 7.

Lemma 7. For $g = 1$ and $U_{max} \geq 1$ (or $r \leq \frac{1}{\sqrt{2}}$), an optimal path without T segments is a concatenation of $|C_\beta G C_\beta|$ and $|C_\beta C_\beta|$ sub-paths, where the start/terminal sub-paths can be truncated.

Proof. As discussed in Remark 8, a path may switch its evolution direction (i.e., clockwise/counter-clockwise) at points $(0, \pm 1)$ and $(\pm \frac{1}{U_{max}}, 0)$. We first show that for $g = 1$ and $U_{max} \geq 1$, any path containing a middle C segment with a switched evolution direction (that is, with the sign of \mathcal{B} changed and the portrait switches direction) is not optimal.

Consider a middle L^- segment with switched evolution direction, as shown in Fig. 12. The L^- segment can be either: (1) entered at $(0, 1)$ from a G^- or R^- segment, and switches direction at $(-\frac{1}{U_{max}}, 0)$; (2) entered at $(-\frac{1}{U_{max}}, 0)$ from a cusp, and switches direction at $(0, 1)$. Notice that in either case, the path remains within the second quadrant in the portrait and represents a L^- segment since the signs of \mathcal{A} and \mathcal{C} do not change. It is clear that the L^- segment is completely traversed twice from opposite directions, therefore its angle is $2 \arctan(\frac{1}{\sqrt{U_{max}^4 - 1}}) + \pi$ according to Lemma 4. Such a L^- segment is visualized in Fig. 13 for $U_{max} = 1.1$ (or $r = \sqrt{2.21}$). However, it is not optimal by Lemma 6. The same conclusion holds for middle L^+ and R segments.

Now consider a middle sub-path that is entered clockwise at the point $(-\frac{1}{U_{max}}, 0)$ from a cusp. Since it has been shown that the middle C segments must not switch their evolution direction on an optimal path, the middle sub-path can only evolve clockwise in the second quadrant, followed by 3 possible cases: (1) entering a G^- segment and then evolving into the right half plane; (2) directly evolving into the right half plane; (3) entering a G^- segment and then evolving back into the left half plane. In any of the cases, the sub-path again completely traverses a C segment until entering a new sub-path at a cusp. The 3 cases are illustrated in Fig. 14, where

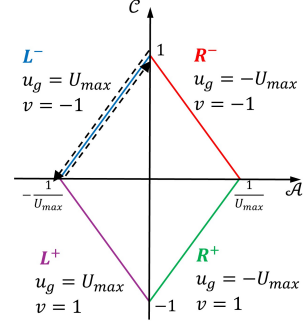


Fig. 12. Illustration of a middle L^- segment with switched evolution directions

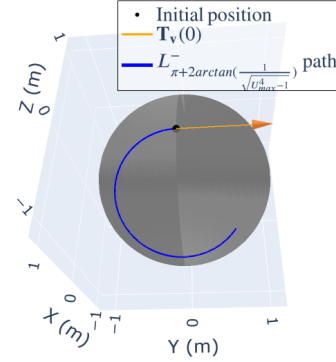


Fig. 13. A middle L^- segment with switched evolution directions on a sphere, for $U_{max} = 1.1$ (or $r = \frac{1}{\sqrt{2.21}}$)

case (2) does not enter the G^- segment in Fig. 14(a). It is clear that cases (1)-(3) correspond to middle sub-paths of type $|L^- G^- R^-|$, $|L^- R^-|$, and $|L^- G^- L^-|$, respectively. The angle of the C segments is $\beta = \arctan(\frac{1}{\sqrt{U_{max}^4 - 1}}) + \frac{\pi}{2}$ by Lemma 4.

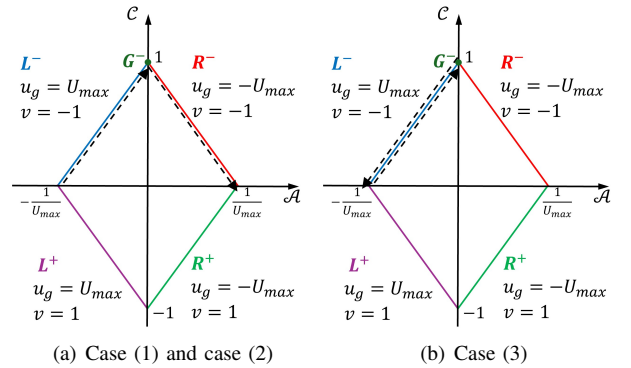


Fig. 14. Illustrative evolution of $\mathcal{A} - \mathcal{C}$ for $g = 1$

Using similar proofs for the middle sub-path entered at $(-\frac{1}{U_{max}}, 0)$ counter-clockwise, and the sub-paths entered at $(\frac{1}{U_{max}}, 0)$ in both clockwise and counter-clockwise directions, it can be proved that the middle sub-paths are of type $|C_\beta G C_\beta|$ or $|C_\beta C_\beta|$. For starting/terminal sub-paths that do not start/terminate at cusps, the starting sub-paths may be truncated to $C G C_\beta|$, $G C_\beta|$, $C_\beta|$, or $C C_\beta|$, with corresponding symmetric forms for the terminal sub-paths. \square

Observing that the key result stated in Lemma 7 leads to an infinite list of potentially optimal path types, we begin by demonstrating the non-optimality and redundancy of certain paths fulfilling these conditions. This allows us to limit the optimal path types to a finite list of sufficient ones.

The following lemma states that $L_\beta|L_\beta$ and $R_\beta|R_\beta$ paths can replace each other, that is, they can connect the same initial and terminal configurations.

Lemma 8. *A $L_\beta^+|L_\beta^-$ path can be replaced by a $R_\beta^+|R_\beta^-$ path, and a $L_\beta^-|L_\beta^+$ path can be replaced by a $R_\beta^-|R_\beta^+$ path, and vice versa.*

Proof. Consider a $L_\beta^+|L_\beta^-$ path and a $R_\beta^+|R_\beta^-$ path with $\beta = \arctan(\frac{1}{\sqrt{U_{max}^4-1}}) + \frac{\pi}{2}$. By (45), it suffices to show that $\mathbf{M}_{L^+}(r, \beta)\mathbf{M}_{L^-}(r, \beta) = \mathbf{M}_{R^+}(r, \beta)\mathbf{M}_{R^-}(r, \beta)$. It can be obtained that $\sin(\arctan(\frac{1}{\sqrt{U_{max}^4-1}})) = \frac{1}{U_{max}^2}$ and $\cos(\arctan(\frac{1}{\sqrt{U_{max}^4-1}})) = \frac{\sqrt{U_{max}^4-1}}{U_{max}^2}$, hence, $\sin(\beta) = \frac{\sqrt{U_{max}^4-1}}{U_{max}^2}$ and $\cos(\beta) = -\frac{1}{U_{max}^2}$. Substituting the value of $\sin(\beta)$, $\cos(\beta)$, and $r = \frac{1}{\sqrt{1+U_{max}^2}}$ into (47), (51), (48), and (52), it is obtained that

$$\begin{aligned} \mathbf{M}_{L^+}(r, \beta)\mathbf{M}_{L^-}(r, \beta) &= \mathbf{M}_{R^+}(r, \beta)\mathbf{M}_{R^-}(r, \beta) \\ &= \begin{pmatrix} \frac{U_{max}^2-2}{U_{max}^2} & \frac{2\sqrt{U_{max}^2-1}}{U_{max}^2} & 0 \\ \frac{2\sqrt{U_{max}^2-1}}{U_{max}^2} & -\frac{U_{max}^2-2}{U_{max}^2} & 0 \\ 0 & 0 & -1 \end{pmatrix}. \end{aligned} \quad (55)$$

With a similar proof for $L_\beta^-|L_\beta^+$ and $R_\beta^-|R_\beta^+$ paths, the lemma is proved. \square

Using Lemma 8, we now prove the non-optimality of a $C_\beta C_\beta|C_\beta$ (or $C_\beta|C_\beta C_\beta$) path.

Lemma 9. *A $C_\beta C_\beta|C_\beta$ (or $C_\beta|C_\beta C_\beta$) path is not optimal.*

Proof. Consider a $L_\beta^- R_\beta^-|R_\beta^+$ path, where $\beta = \arctan(\frac{1}{\sqrt{U_{max}^4-1}}) + \frac{\pi}{2}$. By Lemma 8, the $R_\beta^-|R_\beta^+$ sub-path can be replaced by $L_\beta^-|L_\beta^+$. Hence, an alternative $L_\beta^-|L_\beta^+$ path of the same length as the original $L_\beta^- R_\beta^-|R_\beta^+$ path is constructed. By Lemma 6, the alternate path is not optimal; hence, the $L_\beta^- R_\beta^-|R_\beta^+$ path is not optimal.

The non-optimality of $L_\beta^- R_\beta^-|R_\beta^+$ is visualized in Fig. 15 for $U_{max} = 3$ (or $r = \frac{1}{\sqrt{10}}$).

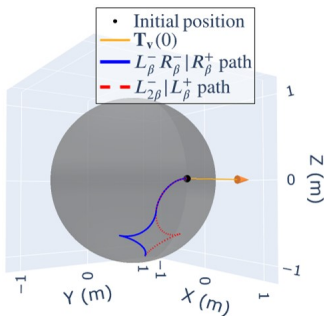


Fig. 15. Non-optimality of $L_\beta^- R_\beta^-|R_\beta^+$

Using similar proofs for paths $L_\beta^+ R_\beta^+|R_\beta^-$, $R_\beta^- L_\beta^-|L_\beta^+$, and $R_\beta^+ L_\beta^+|L_\beta^-$, the lemma is proved. \square

The following lemma states that with any non-negative σ , $G_\sigma C_\beta|C_\beta$ and $C_\beta|C_\beta G_\sigma$ paths can replace each other.

Lemma 10. *A path of type $G_\sigma C_\beta|C_\beta$ can be replaced by a path of type $C_\beta|C_\beta G_\sigma$, and vice versa.*

Proof. Suppose a path is of type $G_\sigma^- L_\beta^-|L_\beta^+$ with $\beta = \arctan(\frac{1}{\sqrt{U_{max}^4-1}}) + \frac{\pi}{2}$ and $\sigma \geq 0$. Suppose that it can be replaced by a path of type $L_\beta^-|L_\beta^+ G_\sigma^+$. It suffices to show that $\mathbf{M}_{L^-}(r, \beta)\mathbf{M}_{L^+}(r, \beta)\mathbf{M}_{G^+}(\sigma) = \mathbf{M}_{G^-}(\sigma)\mathbf{M}_{L^-}(r, \beta)\mathbf{M}_{L^+}(r, \beta)$. As shown in the proof of Lemma 8, $\sin(\beta) = \frac{\sqrt{U_{max}^4-1}}{U_{max}^2}$ and $\cos(\beta) = -\frac{1}{U_{max}^2}$. Substituting the values of $\sin(\beta)$, $\cos(\beta)$, and $r = \frac{1}{\sqrt{1+U_{max}^2}}$ into (46), (47), and (51), it is obtained that

$$\begin{aligned} &\mathbf{M}_{L^-}(r, \beta)\mathbf{M}_{L^+}(r, \beta)\mathbf{M}_{G^+}(\sigma) \\ &= \mathbf{M}_{G^-}(\sigma)\mathbf{M}_{L^-}(r, \beta)\mathbf{M}_{L^+}(r, \beta) \\ &= \begin{pmatrix} \xi_1 & \xi_2 & 0 \\ \xi_2 & -\xi_1 & 0 \\ 0 & 0 & -1 \end{pmatrix}, \end{aligned} \quad (56)$$

where $\xi_1 = c(\sigma)\frac{U_{max}^2-2}{U_{max}^2} - s(\sigma)\frac{2\sqrt{U_{max}^2-1}}{U_{max}^2}$ and $\xi_2 = -s(\sigma)\frac{U_{max}^2-2}{U_{max}^2} - c(\sigma)\frac{2\sqrt{U_{max}^2-1}}{U_{max}^2}$.

With similar proofs for path types $G_\sigma^- R_\beta^-|R_\beta^+$, $G_\sigma^+ L_\beta^+|L_\beta^-$, and $G_\sigma^+ R_\beta^+|R_\beta^-$, the lemma is proved. \square

Using Lemma 10, we now prove the non-optimality of a $C_\beta G_\sigma C_\beta|C_\beta$ (or $C_\beta|C_\beta G_\sigma C_\beta$) path.

Lemma 11. *For $\sigma \geq 0$, a path of type $C_\beta G_\sigma C_\beta|C_\beta$ (or $C_\beta|C_\beta G_\sigma C_\beta$) is not optimal.*

Proof. Consider a $R_\beta^- G_\sigma^- L_\beta^-|L_\beta^+$ path, where $\beta = \arctan(\frac{1}{\sqrt{U_{max}^4-1}}) + \frac{\pi}{2}$ and $\sigma \geq 0$. By Lemma 8, the $L_\beta^-|L_\beta^+$ sub-path can be replaced by a $R_\beta^-|R_\beta^+$ sub-path. Therefore, a new path of type $R_\beta^- G_\sigma^- R_\beta^-|R_\beta^+$ can be constructed, which has the same length as the initial path. Furthermore, by Lemma 10, the $G_\sigma^- R_\beta^-|R_\beta^+$ sub-path can be replaced by a $R_\beta^-|R_\beta^+ G_\sigma^+$ sub-path; hence, an alternate $R_\beta^-|R_\beta^+ G_\sigma^+$ path with the same length is constructed. By Lemma 6, the alternate path is not optimal; hence, the initial $R_\beta^- G_\sigma^- L_\beta^-|L_\beta^+$ path is not optimal.

The non-optimality of $R_\beta^- G_\sigma^- L_\beta^-|L_\beta^+$ is visualized in Fig. 16 for $U_{max} = 3$ (or $r = \frac{1}{\sqrt{10}}$) and $\sigma = \frac{\pi}{6}$.

Using similar proofs for the path types $R^+ G^+ L^+|L^-$, $LGL|L$, $RGR|R$, $LGR|R$, and $C|CGC$, the lemma is proved. \square

With Lemmas 7, 9 and 11, a sufficient list of the optimal path types without T segments for $g = 1$ can be obtained. However, it may be further restricted by showing that some of the path types are redundant (i.e., they may be replaced by path types with equivalent lengths but fewer segments).

Lemma 12. *Paths of type $CC_\beta|C_\beta C$, $CC_\beta|C_\beta G$, $CGC_\beta|C_\beta C$, $GC_\beta|C_\beta G$, $CGC_\beta|C_\beta G$, and $CGC_\beta|C_\beta GC$*

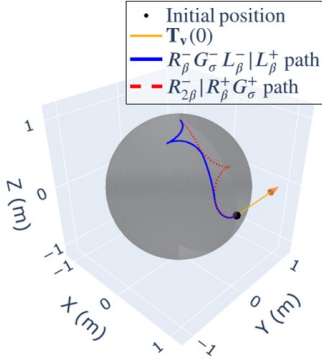


Fig. 16. Non-optimality of $R_\beta^- G_\sigma^- L_\beta^- | L_\beta^+$

are redundant. They may be replaced respectively by paths of type $C|C, C|C_\beta G, CGC_\beta|C, C|C_\beta G, C|C_\beta G,$ and $CGC_\beta|C$.

Proof. The replacement of $CC_\beta|C_\beta C, CC_\beta|C_\beta G,$ and $CGC_\beta|C_\beta C$ paths follows directly from Lemma 8, and the replacement of $GC_\beta|C_\beta G, CGC_\beta|C_\beta G,$ and $CGC_\beta|C_\beta GC$ paths follows directly from Lemmas 8 and 10. \square

B. Optimal Paths Containing T Segments

As shown in the phase portrait in Fig. 9, on an optimal path, an L^0 (or R^0) segment must be preceded and followed by an L (or R) segment. By Lemma 5, these L (or R) segments must be completely traversed if they are middle segments, with arc angles of β , by Lemma 4. Therefore, the optimal path types containing T segments can be easily restricted to a finite sufficient list by showing a path consisting of a T segment and a completely traversed C segment is non-optimal.

As highlighted in Remark 9, for $g = 1$, an optimal path may include T segments solely in the special case of $U_{max} = 1$ (or $r = \frac{1}{\sqrt{2}}$). Hence, $\beta = \arctan(\frac{1}{\sqrt{1-1}}) + \frac{\pi}{2} = \pi$, we have the following lemma.

Lemma 13. For $\rho \geq 0$ and $U_{max} = 1$ (or $r = \frac{1}{\sqrt{2}}$), a $T_\rho C_\pi$ (or $C_\pi T_\rho$) path is not optimal.

Proof. Consider a $L_\rho^0 L_\pi^-$ path, where $\rho \geq 0$. It is claimed that when $U_{max} = 1$, the $L_\rho^0 L_\pi^-$ path can be replaced by an alternate $R_\pi^+ G_\rho^-$ path of equivalent time. From the phase portrait in Fig. 9, an R^+ segment can only be followed by a $G^+, R^0, L^+,$ or R^- segment on an optimal path. Hence, the alternate $R_\pi^+ G_\rho^-$ path is not optimal, indicating the non-optimality of the $L_\rho^0 L_\pi^-$ path.

As one of the paths considered contains a T segment, we must now compare the paths based on time rather than length. We first show that the two paths are of equivalent time. Recall that the time spent on a segment equals $\frac{\phi}{\omega}$, where ϕ and $\omega = \sqrt{v^2 + u_g^2}$ denote the angle and angular frequency of the segment, respectively. Therefore, the time duration spent for a $L_\rho^0 L_\pi^-$ path and a $R_\pi^+ G_\rho^-$ path equal $\frac{\rho}{\sqrt{U_{max}^2}} + \frac{\pi}{\sqrt{1+U_{max}^2}}$ and $\frac{\pi}{\sqrt{1+U_{max}^2}} + \rho$, respectively. These time durations are equivalent when $U_{max} = 1$.

With the equivalence of time shown, it suffices to show that $\mathbf{M}_{L^0}(\rho)\mathbf{M}_{L^-}(\frac{1}{\sqrt{2}}, \pi) = \mathbf{M}_{R^+}(\frac{1}{\sqrt{2}}, \pi)\mathbf{M}_{G^-}(\rho)$. By (48)-(51), we obtain

$$\begin{aligned} \mathbf{M}_{L^0}(\rho)\mathbf{M}_{L^-}(\frac{1}{\sqrt{2}}, \pi) &= \mathbf{M}_{R^+}(\frac{1}{\sqrt{2}}, \pi)\mathbf{M}_{G^-}(\rho) \\ &= \begin{pmatrix} 0 & 0 & -1 \\ s(\rho) & -c(\rho) & 0 \\ -c(\rho) & -s(\rho) & 0 \end{pmatrix}. \end{aligned} \quad (57)$$

The non-optimality of $L_\rho^0 L_\pi^-$ is visualized in Fig. 17 for $\rho = \frac{\pi}{4}$.

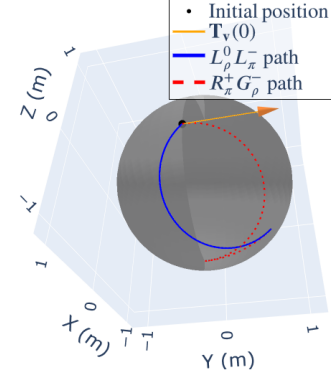


Fig. 17. Non-optimality of $L_\rho^0 L_\pi^-$

Using similar proofs for paths $L_\rho^0 L_\pi^+, R_\rho^0 R_\pi^-,$ and $R_\rho^0 R_\pi^+$, the lemma is proved. \square

Since for $g = 1$ and $U_{max} \geq 1$, an optimal path may include T segments solely when $U_{max} = 1$ (by Remark 9), and a C_π segment corresponds to a middle C segment when $U_{max} = 1$, the following corollary directly follows from Lemma 13.

Corollary 1. For $g = 1$ and $U_{max} \geq 1$ (or $r \leq \frac{1}{\sqrt{2}}$), a path containing a T segment and a middle C segment is not optimal.

Up to this point, all the key results (that is, Lemmas 7, 9, 11, 12, and Corollary 1) are proved, along with detailed proofs of the supporting lemmas.

V. OPTIMAL PATHS FOR $g > 1$

For $g > 1$, as illustrated in Fig. 10, Lemma 16 is the key result that determines the optimal paths as a concatenation. Meanwhile, Lemma 18 serves as the key result that confines the concatenation to a finite list. Below, we enumerate these key results, and their detailed proofs will be provided later in this section.

Remark 11. Throughout this paper, we define the angle $0 < \mu < \arctan(\frac{1}{\sqrt{U_{max}^4-1}}) + \frac{\pi}{2}$, which will be utilized extensively.

Lemma 16. For $g > 1$ and $U_{max} \geq 1$ (or $r \leq \frac{1}{\sqrt{2}}$), the optimal path is a concatenation of $|C_\mu C_\mu|$ sub-paths where the start/terminal sub-paths can be truncated.

Lemma 18. For $U_{max} \geq 1$ (or $r \leq \frac{1}{\sqrt{2}}$), a path of type $C_\mu C_\mu | C_\mu C_\mu$ is not optimal.

Given the above key results, we now prove the main result for $g > 1$, as stated in Proposition 2.

Proposition 2. For $g > 1$ and $U_{max} \geq 1$ (or $r \leq \frac{1}{\sqrt{2}}$), the optimal path may be restricted to the following types, together with their symmetric forms:

$$\begin{aligned} & C, CC, C|C, C|C_\mu C, C|C_\mu C_\mu|C, CC_\mu|C_\mu C, \\ & C|C_\mu C_\mu|C_\mu C, CC_\mu|C_\mu C_\mu|C_\mu C \\ & \text{where } 0 < \mu < \arctan\left(\frac{1}{\sqrt{U_{max}^4 - 1}}\right) + \frac{\pi}{2}. \end{aligned}$$

Proof. For $g > 1$, Lemma 16 dictates that the optimal paths can only be a concatenation of $|C_\mu C_\mu|$ with the start and terminal sub-paths, say P_i and P_f , potentially being truncated. Lemma 18 rules out the optimality of paths containing two or more contiguous middle sub-paths of the form $|C_\mu C_\mu|$. Therefore, the sufficient list of optimal path types consists of the following forms: (a) paths with one full middle sub-path and two truncated start/terminal sub-paths, that is, $P_i|C_\mu C_\mu|P_f$, where $P_i \in \{C, CC_\mu\}$ and $P_f \in \{C, C_\mu C\}$; (b) paths with two truncated start/terminal sub-paths, that is, $P_i|P_f$; and (c) paths with one truncated sub-path, that is, $P_s \in \{C, CC\}$. The union of forms (a), (b), and (c) aligns with the sufficient list provided in Proposition 2. \square

In the remainder of this section, we present comprehensive proofs of the key results utilized above, along with the lemmas that underpin them. The following two lemmas (14 and 15) build the foundation for the proof of the key result in Lemma 16.

Lemma 14. For $g > 1$, the angle of a C segment that is completely traversed clockwise/counter-clockwise is less than $\arctan\left(\frac{1}{\sqrt{U_{max}^4 - 1}}\right) + \frac{\pi}{2}$ radians.

Proof. Similarly to the proof of Lemma 4, (43) can be obtained, which shows that the angle of a completely traversed C segment monotonically decreases as g increases given a fixed U_{max} . Therefore, the angle when $g > 1$ is less than the one when $g = 1$, hence, less than $\arctan\left(\frac{1}{\sqrt{U_{max}^4 - 1}}\right) + \frac{\pi}{2}$. \square

Lemma 15. For $g > 1$ and $U_{max} \geq 1$ (or $r \leq \frac{1}{\sqrt{2}}$), $\mathcal{B} \neq 0$.

Proof. Similarly to the proof of Lemma 5, (44) can be obtained. Therefore, $\mathcal{A}^2 + \mathcal{C}^2$ has a maximum value of 1. Since $\mathcal{A}^2 + \mathcal{B}^2 + \mathcal{C}^2 \equiv g > 1$, \mathcal{B}^2 is always greater than zero, hence, $\mathcal{B} \neq 0$. \square

Using Lemmas 14 and 15, we proceed to prove the key result of Lemma 16.

Lemma 16. For $g > 1$ and $U_{max} \geq 1$ (or $r \leq \frac{1}{\sqrt{2}}$), the optimal path is a concatenation of $|C_\mu C_\mu|$ sub-paths where the start/terminal sub-paths can be truncated.

Proof. By Lemma 15, either $\mathcal{B} > 0$ or $\mathcal{B} < 0$ for an optimal path; consequently, $\frac{d\mathcal{A}}{dt} \neq 0$ when $v \neq 0$ and $\frac{d\mathcal{C}}{dt} \neq 0$ when $u_g \neq 0$. Therefore the path evolves either clockwise or counter-clockwise without entering a G or T segment on the $\mathcal{A} - \mathcal{C}$ portrait by Lemma 3, as shown in Fig. 18. From Fig. 18, it is clear that the optimal path is a concatenation of $|CC|$ sub-paths; for start/terminal sub-paths that do not start/terminate at cusps, they are truncated but the evolution

directions remain the same. Furthermore, it is clear that all middle C segments are completely traversed once, either clockwise or counter-clockwise; hence, they all have an angle of $\mu < \arctan\left(\frac{1}{\sqrt{U_{max}^4 - 1}}\right) + \frac{\pi}{2}$ according to Lemma 14. \square

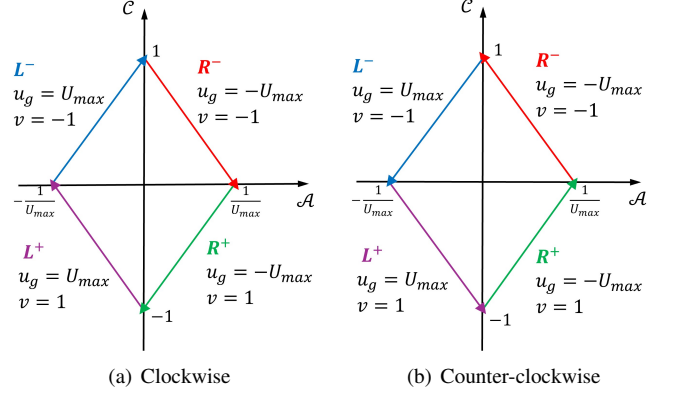


Fig. 18. Evolution of $\mathcal{A} - \mathcal{C}$ for $g > 1$

In the following Lemma 17, we demonstrate that for $0 < \mu < \arctan\left(\frac{1}{\sqrt{U_{max}^4 - 1}}\right) + \frac{\pi}{2}$, there is always an ϵ satisfying $0 < \epsilon < 2\mu$, which allows the construction of a $C_\mu C_\epsilon C_\mu$ path connecting the same start and terminal configurations as some G path. This result will become useful for proving the key result Lemma 18.

Lemma 17. For $U_{max} \geq 1$ (or $r \leq \frac{1}{\sqrt{2}}$), there exists an ϵ such that $0 < \epsilon < 2\mu$ and a $C_\mu^+ C_\epsilon^+ C_\mu^+$ (or $C_\mu^- C_\epsilon^- C_\mu^-$) path can be replaced by a G_θ^+ (or G_θ^-) path.

Proof. Consider a $L_\mu^+ R_\epsilon^+ L_\mu^+$ path where $0 < \mu < \arctan\left(\frac{1}{\sqrt{U_{max}^4 - 1}}\right) + \frac{\pi}{2}$. For it to be replaced by a G_θ^+ path, the following equation must be satisfied:

$$\mathbf{M}_{L^+}(r, \mu) \mathbf{M}_{R^+}(r, \epsilon) \mathbf{M}_{L^+}(r, \mu) = \mathbf{M}_{G^+}(\theta). \quad (58)$$

We utilize the following axial vectors for the characterization of ϵ :

$$\mathbf{u}_{L^+} := (\sqrt{1 - r^2}, 0, r)^T, \mathbf{u}_{R^+} := (-\sqrt{1 - r^2}, 0, r)^T, \quad (59)$$

where \mathbf{u}_{L^+} and \mathbf{u}_{R^+} are the axial vectors of $\mathbf{M}_{L^+}(r, \cdot)$ and $\mathbf{M}_{R^+}(r, \cdot)$, respectively. Therefore, $\mathbf{M}_{L^+}(r, \mu) \mathbf{u}_{L^+} = \mathbf{u}_{L^+}$, $\mathbf{u}_{L^+}^T \mathbf{M}_{L^+}(r, \mu) = \mathbf{u}_{L^+}^T$, $\mathbf{M}_{R^+}(r, \mu) \mathbf{u}_{R^+} = \mathbf{u}_{R^+}$, and $\mathbf{u}_{R^+}^T \mathbf{M}_{R^+}(r, \mu) = \mathbf{u}_{R^+}^T$.

By pre-multiplying both sides of (58) with $\mathbf{u}_{L^+}^T$ and post-multiplying with \mathbf{u}_{L^+} , it is obtained that:

$$\mathbf{u}_{L^+}^T \mathbf{M}_{R^+}(r, \epsilon) \mathbf{u}_{L^+} = \mathbf{u}_{L^+}^T \mathbf{M}_{G^+}(\theta) \mathbf{u}_{L^+}. \quad (60)$$

By further substituting (46), (48) and (59) into (60), it is obtained that:

$$r^2 - c(\theta)(r^2 - 1) = (4r^2 - 4r^4)(c(\epsilon) - 1) + 1. \quad (61)$$

Similarly, by pre-multiplying both sides of (58) with $\mathbf{u}_{L^+}^T$ and post-multiplying with \mathbf{u}_{R^+} , it is obtained that:

$$\begin{aligned} & r^2 + c(\theta)(r^2 - 1) \\ &= (4r^2 - 4r^4) \left(c(\mu)(-1 + 2r^2) + s(\mu)s(\epsilon) + c(\epsilon)(-1 + 2r^2) \right. \\ & \quad \left. + c(\mu)c(\epsilon)(1 - 2r^2) + 1 - 2r^2 \right) + 2r^2 - 1. \end{aligned} \quad (62)$$

By taking the sum of (61) and (62) on both sides and utilizing the fact that $4r^2 - 4r^4 \neq 0$ for $r \leq \frac{1}{\sqrt{2}}$, we obtain:

$$c(\epsilon) \left(c(\mu)(1 - 2r^2) + 2r^2 \right) + s(\epsilon)s(\mu) = c(\mu)(1 - 2r^2) + 2r^2. \quad (63)$$

We now divide each side of the above equation by $\sqrt{(c(\mu)(1 - 2r^2) + 2r^2)^2 + s^2(\mu)}$, noting that this quantity is non-zero. This is justified since $s^2(\mu) > 0$ for $0 < \mu < \arctan\left(\frac{1}{\sqrt{U_{max}^4 - 1}}\right) + \frac{\pi}{2} \leq \pi$. Furthermore, defining $c(\delta) := \frac{c(\mu)(1 - 2r^2) + 2r^2}{\sqrt{(c(\mu)(1 - 2r^2) + 2r^2)^2 + s^2(\mu)}}$ and $s(\delta) := \frac{s(\mu)}{\sqrt{(c(\mu)(1 - 2r^2) + 2r^2)^2 + s^2(\mu)}}$, (63) can be rewritten as:

$$c(\epsilon - \delta) = c(\delta). \quad (64)$$

Therefore,

$$\epsilon = c^{-1}(c(\delta)) + \delta. \quad (65)$$

It is worth noting that $c^{-1}(c(\delta))$ has two possible values within $[0, 2\pi]$, namely, δ and $2\pi - \delta$, we next prove that it can only be equal to δ . Suppose $s(c^{-1}(c(\delta))) = s(2\pi - \delta) = -s(\delta)$, then $c(\epsilon) = c(\delta)c(c^{-1}(c(\delta))) - s(\delta)s(c^{-1}(c(\delta))) = c^2(\delta) + s^2(\delta) = 1$. Since it is defined that $0 < \epsilon < 2\mu < 2\pi$, this is not possible. Hence, $s(c^{-1}(c(\delta))) = s(\delta)$. Therefore, $c^{-1}(c(\delta)) = \delta$, and by (65) we obtain $\epsilon = 2\delta$.

Next, we will show that $0 < \epsilon = 2\delta < 2\mu$. Since $0 < \mu < \arctan\left(\frac{1}{\sqrt{U_{max}^4 - 1}}\right) + \frac{\pi}{2} \leq \pi$, $s(\mu) > 0$. Therefore, $s(\delta) = \frac{s(\mu)}{\sqrt{(c(\mu)(1 - 2r^2) + 2r^2)^2 + s^2(\mu)}} > 0$, hence, $0 < \delta < \pi$. We further compare δ with μ by taking their difference:

$$\begin{aligned} s(\mu - \delta) &= s(\mu)c(\delta) - c(\mu)s(\delta) \\ &= \frac{s(\mu) \left(c(\mu)(1 - 2r^2) + 2r^2 \right) - c(\mu)s(\mu)}{\sqrt{(c(\mu)(1 - 2r^2) + 2r^2)^2 + s^2(\mu)}} \\ &= \frac{2r^2 s(\mu) (1 - c(\mu))}{\sqrt{(c(\mu)(1 - 2r^2) + 2r^2)^2 + s^2(\mu)}}. \end{aligned} \quad (66)$$

Since $0 < \mu < \arctan\left(\frac{1}{\sqrt{U_{max}^4 - 1}}\right) + \frac{\pi}{2} \leq \pi$, $s(\mu) > 0$ and $-1 < c(\mu) < 1$. Hence, $s(\mu - \delta) > 0$. Furthermore, since $0 < \delta < \pi$, $\mu - \delta > 0$. Hence, $\mu > \delta > 0$, and $0 < \epsilon = 2\delta < 2\mu$.

Substituting $c(\epsilon) = c(2\delta) = c^2(\delta) - s^2(\delta)$ and $s(\epsilon) = s(2\delta) = 2s(\delta)c(\delta)$ into (58), it can be checked that:

$$\begin{aligned} \mathbf{M}_{G^+}(\theta) &= \mathbf{M}_{L^+}(r, \mu) \mathbf{M}_{R^+}(r, \epsilon) \mathbf{M}_{L^+}(r, \mu) \\ &= \begin{pmatrix} c(\theta) & -s(\theta) & 0 \\ s(\theta) & c(\theta) & 0 \\ 0 & 0 & 1 \end{pmatrix}, \end{aligned} \quad (67)$$

where $c(\theta) = \frac{(4r^2 - 8r^4)c(\mu) + (4r^2 + 4r^4)c^2(\mu) - 8r^2 + 4r^4 + 1}{(4r^2 - 8r^4)c(\mu) + (-4r^2 + 4r^4)c^2(\mu) + 4r^4 + 1}$ and $s(\theta) = \frac{4r((1 - 2r^2)s(\mu) + 2r^2c(\mu)s(\mu))}{(4r^2 - 8r^4)c(\mu) + (-4r^2 + 4r^4)c^2(\mu) + 4r^4 + 1}$.

Visualizations of a G_θ^+ path replacing a $L_\mu^+ R_\epsilon^+ L_\mu^+$ path are shown in Fig. 19 for $\mu = \frac{\pi}{3}$ and $\mu = \frac{2\pi}{3}$. In both cases, $U_{max} = 3$ (or $r = \frac{1}{\sqrt{10}}$) and the corresponding values of ϵ and θ are calculated.

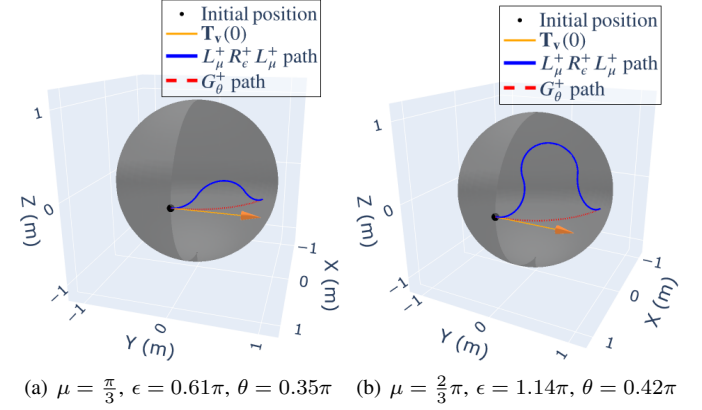


Fig. 19. Replacing a $L_\mu^+ R_\epsilon^+ L_\mu^+$ path with a G_θ^+ path

With similar proofs for $R_\mu^+ L_\epsilon^+ R_\mu^+$, $L_\mu^- R_\epsilon^- L_\mu^-$, and $R_\mu^- L_\epsilon^- R_\mu^-$ paths, the lemma is proved. \square

Now, utilizing Lemma 17, the key result Lemma 18 can be proved.

Lemma 18. For $U_{max} \geq 1$ (or $r \leq \frac{1}{\sqrt{2}}$), a path of type $C_\mu C_\mu | C_\mu C_\mu$ is not optimal.

Proof. Consider a $R_\mu^+ L_\mu^+ | L_\mu^- R_\mu^-$ path where $0 < \mu < \arctan\left(\frac{1}{\sqrt{U_{max}^4 - 1}}\right) + \frac{\pi}{2}$. It is claimed that there exists an alternate $L^- R^- | R^+ L^+$ or $R^+ | R^- | R^+ | R^-$ path that is shorter.

By Lemma 17,

$$\mathbf{M}_{L^+}(r, \mu) \mathbf{M}_{R^+}(r, \epsilon) \mathbf{M}_{L^+}(r, \mu) = \mathbf{M}_{G^+}(\theta), \quad (68)$$

$$\mathbf{M}_{L^-}(r, \mu) \mathbf{M}_{R^-}(r, \epsilon) \mathbf{M}_{L^-}(r, \mu) = \mathbf{M}_{G^-}(\theta). \quad (69)$$

From (46)-(52), it is clear that each of them is an orthogonal matrix, and it can be checked that $\mathbf{M}_{G^+}(\phi) = \mathbf{M}_{G^-}^{-1}(\phi)$, $\mathbf{M}_{L^+}(r, \phi) = \mathbf{M}_{R^-}^{-1}(r, \phi)$, and $\mathbf{M}_{R^+}(r, \phi) = \mathbf{M}_{L^-}^{-1}(r, \phi)$. By post-multiplying the two sides of (68) with the two sides of (69), respectively, it is obtained that:

$$\begin{aligned} & \mathbf{M}_{L^+}(r, \mu) \mathbf{M}_{R^+}(r, \epsilon) \mathbf{M}_{L^+}(r, \mu) \mathbf{M}_{L^-}(r, \mu) \mathbf{M}_{R^-}(r, \epsilon) \\ & \cdot \mathbf{M}_{L^-}(r, \mu) = \mathbf{I}_3, \end{aligned} \quad (70)$$

where \mathbf{I}_3 is the identity matrix. Further pre-multiplying $\mathbf{M}_{R^-}(r, \mu)$ and post-multiplying $\mathbf{M}_{R^+}(r, \mu) \mathbf{M}_{L^+}(r, \epsilon)$ on both sides:

$$\begin{aligned} & \mathbf{M}_{R^+}(r, \epsilon) \mathbf{M}_{L^+}(r, \mu) \mathbf{M}_{L^-}(r, \mu) \\ & = \mathbf{M}_{R^-}(r, \mu) \mathbf{M}_{R^+}(r, \mu) \mathbf{M}_{L^+}(r, \epsilon), \end{aligned} \quad (71)$$

this can be rewritten as:

$$\begin{aligned} & \mathbf{M}_{R^+}(r, \epsilon - \mu + \mu) \mathbf{M}_{L^+}(r, \mu) \mathbf{M}_{L^-}(r, \mu) \\ & = \mathbf{M}_{R^-}(r, \mu) \mathbf{M}_{R^+}(r, \mu) \mathbf{M}_{L^+}(r, \epsilon - \mu + \mu), \end{aligned} \quad (72)$$

pre-multiplying $\mathbf{M}_{L^-}(r, \epsilon - \mu)$ and post-multiplying $\mathbf{M}_{R^-}(r, \mu)$ on both sides of the above equation:

$$\begin{aligned} & \mathbf{M}_{R^+}(r, \mu)\mathbf{M}_{L^+}(r, \mu)\mathbf{M}_{L^-}(r, \mu)\mathbf{M}_{R^-}(r, \mu) \\ &= \mathbf{M}_{L^-}(r, \epsilon - \mu)\mathbf{M}_{R^-}(r, \mu)\mathbf{M}_{R^+}(r, \mu)\mathbf{M}_{L^+}(r, \epsilon - \mu). \end{aligned} \quad (73)$$

From Lemma 17, $0 < \epsilon < 2\mu$. If $\epsilon \geq \mu$, then $\mu > \epsilon - \mu \geq 0$. Hence, by (73), there exists an alternate $L_{\epsilon-\mu}^- R_{\mu}^- | R_{\mu}^+ L_{\epsilon-\mu}^+$ (or $R_{\mu}^- | R_{\mu}^+$ if $\epsilon = \mu$) path that is shorter than the $R_{\mu}^+ L_{\mu}^+ | L_{\mu}^- R_{\mu}^-$ path.

If $\epsilon < \mu$, then $0 > \epsilon - \mu > -\mu$. Noting that $\mathbf{M}_{L^-}(r, \epsilon - \mu) = \mathbf{M}_{R^+}(r, \mu - \epsilon)$ and $\mathbf{M}_{L^+}(r, \epsilon - \mu) = \mathbf{M}_{R^-}(r, \mu - \epsilon)$, (73) can be rewritten as:

$$\begin{aligned} & \mathbf{M}_{R^+}(r, \mu)\mathbf{M}_{L^+}(r, \mu)\mathbf{M}_{L^-}(r, \mu)\mathbf{M}_{R^-}(r, \mu) \\ &= \mathbf{M}_{R^+}(r, \mu - \epsilon)\mathbf{M}_{R^-}(r, \mu)\mathbf{M}_{R^+}(r, \mu)\mathbf{M}_{R^-}(r, \mu - \epsilon), \end{aligned} \quad (74)$$

where $\mu > \mu - \epsilon > 0$. Hence, there exists an alternate $R_{\mu-\epsilon}^+ | R_{\mu}^- | R_{\mu}^+ | R_{\mu-\epsilon}^-$ path that is shorter than the $R_{\mu}^+ L_{\mu}^+ | L_{\mu}^- R_{\mu}^-$ path.

The non-optimality of $R_{\mu}^+ L_{\mu}^+ | L_{\mu}^- R_{\mu}^-$ is visualized in Fig. 20 for two cases: (a) $\mu = \frac{\pi}{2}$ and $U_{max} = 3$ (or $r = \frac{1}{\sqrt{10}}$); (b) $\mu = \frac{3}{4}\pi$ and $U_{max} = 1.1$ (or $r = \frac{1}{\sqrt{2.21}}$). In these cases, the alternate shorter paths are $L_{\epsilon-\mu}^- R_{\mu}^- | R_{\mu}^+ L_{\epsilon-\mu}^+$ and $R_{\mu-\epsilon}^+ | R_{\mu}^- | R_{\mu}^+ | R_{\mu-\epsilon}^-$, respectively.

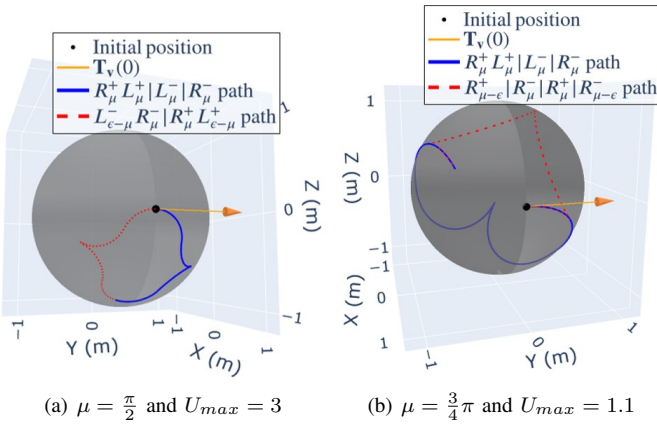


Fig. 20. Non-optimality of $R_{\mu}^+ L_{\mu}^+ | L_{\mu}^- R_{\mu}^-$

With similar proofs for $R_{\mu}^- L_{\mu}^- | L_{\mu}^+ R_{\mu}^+$, $L_{\mu}^+ R_{\mu}^+ | R_{\mu}^- L_{\mu}^-$, and $L_{\mu}^- R_{\mu}^- | R_{\mu}^+ L_{\mu}^+$ paths, the lemma is proved. \square

With the key results, Lemmas 16 and 18, the finite sufficient list for $g > 1$ listed in Proposition 2 can be obtained.

VI. OPTIMAL PATHS FOR $g < 1$

Referring to Fig. 10, for $g < 1$, Lemma 19 alone adequately indicates the main result.

For $\mathcal{A}^2 + \mathcal{B}^2 + \mathcal{C}^2 \equiv g < 1$, an extremal path never reaches $(0, 1)$ or $(0, -1)$ in Fig. 9. Hence, it only evolves within the left or right half plane in Fig. 9, and $u_g \equiv \pm U_{max}$ since \mathcal{A} does not change sign. From (25), $\frac{d\mathcal{C}}{dt} = -U_{max}\mathcal{B}$. By squaring both sides and utilizing (36), we obtain $(\frac{d\mathcal{C}}{dt})^2 = U_{max}^2(g^2 - \mathcal{A}^2 - \mathcal{C}^2)$. Substituting \mathcal{A}^2 by means of (29), wherein $\mathcal{A} =$

$\frac{1-|\mathcal{C}|}{\pm U_{max}}$, results in $(\frac{d\mathcal{C}}{dt})^2 = U_{max}^2(g^2 - \frac{1+|\mathcal{C}|^2-2|\mathcal{C}|}{U_{max}^2} - \mathcal{C}^2)$. By reorganizing the equation, the relationship between $\mathcal{C}(t)$ and $\frac{d\mathcal{C}(t)}{dt}$ is established as:

$$\left(|\mathcal{C}(t)| - \frac{1}{1+U_{max}^2}\right)^2 + \frac{1}{1+U_{max}^2} \left(\frac{d\mathcal{C}(t)}{dt}\right)^2 = \lambda_c^2, \quad (75)$$

where $\lambda_c^2 = \frac{U_{max}^2 g^2 - 1}{1+U_{max}^2} + \frac{1}{(1+U_{max}^2)^2}$. Using the above equation and (28), the phase portrait of $\mathcal{C}(t)$ is shown in Fig. 21. Note that $\lambda_c \geq 0$, and since an extremal path never reaches $(0, 1)$ or $(0, -1)$ in Fig. 9 for $g < 1$, $\mathcal{C}(t) < 1$ in Fig. 21; hence, $\lambda_c < \sqrt{\left(1 - \frac{1}{1+U_{max}^2}\right)^2 + 0} = \frac{U_{max}^2}{1+U_{max}^2}$. Furthermore, for the phase portrait to intersect with the $\frac{d\mathcal{C}}{dt}$

axis, $\lambda_c \geq \sqrt{\left(0 - \frac{1}{1+U_{max}^2}\right)^2 + 0} = \frac{1}{1+U_{max}^2}$.

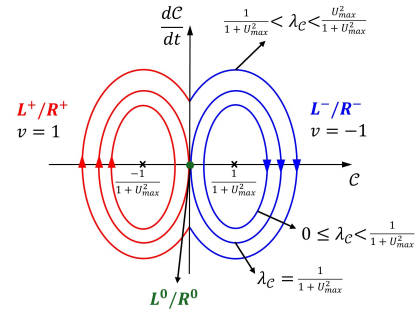


Fig. 21. Phase portrait of $\mathcal{C} - \frac{d\mathcal{C}}{dt}$ for $g < 1$

The key result Lemma 19 can be obtained by directly utilizing the phase portrait of $\mathcal{C}(t)$.

Lemma 19. For $g < 1$ and $U_{max} \geq 1$ (or $r \leq \frac{1}{\sqrt{2}}$), the optimal path is of type C , T , TC (or CT), or a concatenation of C segments joined by cusps or joined by T segments, and any path containing a middle C segment is not optimal.

Proof. From the phase portrait shown by Fig. 21, it is clear that for $0 \leq \lambda_c < \frac{1}{1+U_{max}^2}$, a nontrivial extremal path is a C path. For $\frac{1}{1+U_{max}^2} < \lambda_c < \frac{U_{max}^2}{1+U_{max}^2}$, it is a concatenation of C segments joined by cusps, with each middle C segment traversing the left or right half plane exactly once. For $\lambda_c = \frac{1}{1+U_{max}^2}$, it is either a T path, a TC (or CT) path, or a concatenation of C segments. Between two consecutive C segments, if a path remains at the origin in Fig. 21 for some duration, the C segments are joined by a T segment; otherwise, they are joined by a cusp. Furthermore, the middle C segments traverse the left or right half plane at least once (if a middle C segment passes through the origin instantly without transitioning into another half plane, it traverses the same half plane at least twice).

Now we prove that any path containing a middle C segment is not optimal. Given that a middle C segment traverses the left or right half plane at least once, as established in the above discussion, it is sufficient to demonstrate the non-optimality of a middle C segment that traverses the left or right half plane just once. Consider such a segment of type C^- and let t_2 denote the time spent on it. From Fig. 21, on the C^- segment, $\mathcal{C}(0) = \mathcal{C}(t_2) = 0$. By (75),

$\frac{dC}{dt}(0) = \sqrt{\frac{(1+U_{max}^2)^2\lambda_C^2-1}{1+U_{max}^2}} = -\frac{dC}{dt}(t_2)$. Further, by (34) and (35), on the middle C^- segment,

$$C(0) = \lambda_C \sin(-\phi_C) + \frac{1}{1+U_{max}^2} = 0, \quad (76)$$

$$\begin{aligned} \frac{dC}{dt}(0) &= \lambda_C \sqrt{1+U_{max}^2} \cos(-\phi_C) \\ &= \sqrt{\frac{(1+U_{max}^2)^2\lambda_C^2-1}{1+U_{max}^2}}, \end{aligned} \quad (77)$$

$$C(t_2) = \lambda_C \sin(\sqrt{1+U_{max}^2}t_2 - \phi_C) + \frac{1}{1+U_{max}^2} = 0, \quad (78)$$

$$\begin{aligned} \frac{dC}{dt}(t_2) &= \lambda_C \sqrt{1+U_{max}^2} \cos(\sqrt{1+U_{max}^2}t_2 - \phi_C) \\ &= -\sqrt{\frac{(1+U_{max}^2)^2\lambda_C^2-1}{1+U_{max}^2}}. \end{aligned} \quad (79)$$

Hence, $\lambda_C \sin(-\phi_C) = -\frac{1}{1+U_{max}^2}$, $\lambda_C \cos(-\phi_C) = \sqrt{\frac{(1+U_{max}^2)^2\lambda_C^2-1}{(1+U_{max}^2)^2}}$, $\lambda_C \sin(\sqrt{1+U_{max}^2}t_2 - \phi_C) = -\frac{1}{1+U_{max}^2}$, $\lambda_C \cos(\sqrt{1+U_{max}^2}t_2 - \phi_C) = -\sqrt{\frac{(1+U_{max}^2)^2\lambda_C^2-1}{(1+U_{max}^2)^2}}$. Therefore,

$$t_2 = \frac{\pi + 2 \arctan\left(\frac{1}{\sqrt{(1+U_{max}^2)^2\lambda_C^2-1}}\right)}{\sqrt{1+U_{max}^2}}. \quad (80)$$

Let α_2 and ω_2 denote the arc angle and angular frequency of the C^- segment. Note that $\alpha_2 = \omega_2 t_2$, and $\omega_2 = \sqrt{1+U_{max}^2}$. Therefore,

$$\alpha_2 = \pi + 2 \arctan\left(\frac{1}{\sqrt{(1+U_{max}^2)^2\lambda_C^2-1}}\right), \quad (81)$$

which is a function that monotonically decreases as λ_C^2 increases given a fixed U_{max} . For a path that contains a middle C segment, it must be satisfied that $\frac{1}{1+U_{max}^2} \leq \lambda_C < \frac{U_{max}^2}{1+U_{max}^2}$. Therefore, by (81), $\pi + 2 \arctan\left(\frac{1}{\sqrt{U_{max}^4-1}}\right) < \alpha_2 \leq 2\pi$, which is not optimal directly following Lemma 6.

With a similar proof for middle segments of type C^+ , the lemma is proved. \square

With Lemma 19, we can directly prove the main result for $g < 1$, as listed in Proposition 3 below.

Proposition 3. For $g < 1$ and $U_{max} \geq 1$ (or $r \leq \frac{1}{\sqrt{2}}$), the optimal path may be restricted to the following types, together with their symmetric forms: C , T , $C|C$, TC , CTC .

Proof. According to Lemma 19, for $g < 1$, no path that contains a middle C segment is optimal, thus ruling out paths that contain more than two C segments. Therefore, within the possible forms by Lemma 19, the only paths left are C , T , TC (or CT), and the paths with two C segments joined by a cusp or a T segment, namely, $C|C$ and CTC . \square

With Propositions 1-3, the full sufficient list is characterized:

Theorem 1. For $U_{max} \geq 1$ (or $r \leq \frac{1}{\sqrt{2}}$), the optimal path may be restricted to the following types, together with their symmetric forms:

C , G , T , CC , GC , $C|C$, TC ,
 $CC_\psi|C$, CGC , $C|C_\beta G$, CTC ,
 $C|C_\psi C_\psi|C$, $CGC_\beta|C$, $CC_\mu|C_\mu C$,
 $C|C_\beta GC_\beta|C$, $C|C_\mu C_\mu|C_\mu C$, $CC_\mu|C_\mu C_\mu|C_\mu C$,
 where $0 < \psi \leq \arctan(\frac{1}{\sqrt{U_{max}^4-1}}) + \frac{\pi}{2}$, $\beta = \arctan(\frac{1}{\sqrt{U_{max}^4-1}}) + \frac{\pi}{2}$, and $0 < \mu < \arctan(\frac{1}{\sqrt{U_{max}^4-1}}) + \frac{\pi}{2}$.

VII. PATH GENERATION AND NUMERICAL EXAMPLE

With the sufficient list of optimal path types, candidate solutions for each path need to be generated through inverse kinematics, given an initial configuration, a desired terminal configuration, and an U_{max} (or r). To this end, we make use of the rotation matrices in (46)-(53) and their corresponding axial vectors to derive closed-form expressions for the angles of each path in the sufficient list. With the candidate solutions generated, the feasible paths can be readily identified by verifying if the candidates connect the initial and desired terminal configuration through forward kinematics. Subsequently, the optimal path can be found by comparing the time across all feasible paths. A separate note for the generation of candidate paths, along with the source code for solving the time-optimal spherical CRS problem and visualization, is available at <https://github.com/sixuli97/Optimal-Spherical-Convexified-Reeds-Shepp-Paths>.

In the following numerical example, the initial configuration is set to be $\mathbf{R}(0) = \mathbf{I}_3$, and $U_{max} = 3$ (or $r = \frac{1}{\sqrt{10}}$). The desired terminal configuration is randomly generated as

$$\mathbf{R}(T) = \begin{pmatrix} 0.804977 & -0.592216 & 0.035944 \\ -0.569461 & -0.754203 & 0.326943 \\ -0.166512 & -0.283650 & -0.944360. \end{pmatrix} \quad (82)$$

The feasible paths are summarized in Table I. By comparing the third column, it is clear that the $R^-R^+G^+L^+$ path is time-optimal. The paths are visualized in Fig. 22.

TABLE I
FEASIBLE PATHS

Path type	Angles (rad)	Time (s)
$L^-R^-R^+$	[0.1122, 1.4896, 1.6238]	1.0200
$L^-L^0L^+$	[1.2685, 1.3659, 0.9832]	1.1673
$L^-R^-R^+L^+$	[2.4701, 0.5045, 0.5045, 2.1848]	1.7911
$R^+L^+L^-R^-$	[2.5273, 1.5573, 1.5573, 2.8126]	2.6735
$R^-R^+G^+L^+$	[1.4008, 1.6821, 0.0160, 0.0864]	1.0182

VIII. CONCLUSION

This paper addresses the time-optimal path problem of the convexified Reeds-Shepp vehicle (CRS) on a unit sphere. The spherical CRS vehicle is modeled as a variant of the Dubins vehicle in the Sabban frame, with considerations for constrained turning rate and speed. The problem can be used for optimal attitude control of underactuated satellites, optimal motion planning for spherical rolling robots, and optimal

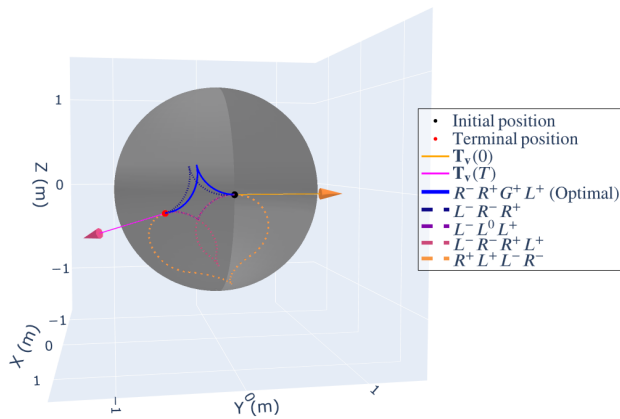


Fig. 22. Optimal and feasible paths connecting the initial and desired terminal configurations

path planning for mobile robots on spherical surfaces or uneven terrains. To solve the proposed problem, the Pontryagin maximum principle is utilized, along with the analysis of phase portraits of the Hamiltonians. Furthermore, detailed proofs of the non-optimality or redundancy of certain path types are established, ultimately leading to the derivation of a sufficient list of optimal path types for $U_{max} \geq 1$ (or $r \leq \frac{1}{\sqrt{2}}$).

This sufficient list includes 23 path types, each composed of at most 6 segments, ensuring a thorough exploration of possible optimal paths given the start and desired terminal configurations. Furthermore, closed-form expressions for the angles of each path in the sufficient list are derived, and the source code for solving the time-optimal path problem is released publicly online.

REFERENCES

- [1] D. J. Balkcom, P. A. Kavathekar, and M. T. Mason, "Time-optimal trajectories for an omni-directional vehicle," *The International Journal of Robotics Research*, vol. 25, no. 10, pp. 985–999, 2006.
- [2] E. Frazzoli, M. A. Dahleh, and E. Feron, "Maneuver-based motion planning for nonlinear systems with symmetries," *IEEE transactions on robotics*, vol. 21, no. 6, pp. 1077–1091, 2005.
- [3] M. W. Mueller, M. Hehn, and R. D'Andrea, "A computationally efficient motion primitive for quadcopter trajectory generation," *IEEE transactions on robotics*, vol. 31, no. 6, pp. 1294–1310, 2015.
- [4] L. E. Dubins, "On curves of minimal length with a constraint on average curvature, and with prescribed initial and terminal positions and tangents," *American Journal of mathematics*, vol. 79, no. 3, pp. 497–516, 1957.
- [5] J. Reeds and L. Shepp, "Optimal paths for a car that goes both forwards and backwards," *Pacific journal of mathematics*, vol. 145, no. 2, pp. 367–393, 1990.
- [6] L. S. Pontryagin, *Mathematical theory of optimal processes*. Routledge, 2018.
- [7] J.-D. Boissonnat, A. Cérézo, and J. Leblond, "Shortest paths of bounded curvature in the plane," *Journal of Intelligent and Robotic Systems*, vol. 11, pp. 5–20, 1994.
- [8] H. J. Sussmann and G. Tang, "Shortest paths for the reeds-shepp car: a worked out example of the use of geometric techniques in nonlinear optimal control," *Rutgers Center for Systems and Control Technical Report*, vol. 10, pp. 1–71, 1991.
- [9] H. Chitsaz, S. M. LaValle, D. J. Balkcom, and M. T. Mason, "Minimum wheel-rotation paths for differential-drive mobile robots," *The International Journal of Robotics Research*, vol. 28, no. 1, pp. 66–80, 2009.
- [10] C. Y. Kaya, "Markov–dubins path via optimal control theory," *Computational Optimization and Applications*, vol. 68, no. 3, pp. 719–747, 2017.
- [11] F. Monroy-Pérez, "Non-euclidean dubins' problem," *Journal of dynamical and control systems*, vol. 4, pp. 249–272, 1998.
- [12] D. P. Kumar, S. Darbha, S. G. Manyam, and D. Casbeer, "The weighted markov-dubins problem," *IEEE Robotics and Automation Letters*, vol. 8, no. 3, pp. 1563–1570, 2023.
- [13] D. J. Balkcom and M. T. Mason, "Time optimal trajectories for bounded velocity differential drive vehicles," *The International Journal of Robotics Research*, vol. 21, no. 3, pp. 199–217, 2002.
- [14] J. Z. Ben-Asher and E. D. Rimon, "Time optimal trajectories for a car-like mobile robot," *IEEE Transactions on Robotics*, vol. 38, no. 1, pp. 421–432, 2021.
- [15] H. J. Sussmann, "Shortest 3-dimensional paths with a prescribed curvature bound," in *Proceedings of 1995 34th IEEE Conference on Decision and Control*, vol. 4. IEEE, 1995, pp. 3306–3312.
- [16] H. Chitsaz and S. M. LaValle, "Time-optimal paths for a dubins airplane," in *2007 46th IEEE conference on decision and control*. IEEE, 2007, pp. 2379–2384.
- [17] Y. Chitour and M. Sigalotti, "Dubins' problem on surfaces. i. nonnegative curvature," *The Journal of Geometric Analysis*, vol. 15, pp. 565–587, 2005.
- [18] S. Darbha, A. Pavan, R. Kumbakonam, S. Rathinam, D. W. Casbeer, and S. G. Manyam, "Optimal geodesic curvature constrained dubins' paths on a sphere," *Journal of Optimization Theory and Applications*, vol. 197, no. 3, pp. 966–992, 2023.
- [19] D. P. Kumar, S. Darbha, S. G. Manyam, and D. Casbeer, "Generalization of optimal geodesic curvature constrained dubins' path on sphere with free terminal orientation," *IEEE Control Systems Letters*, 2024.
- [20] Y. Yoshimura, T. Matsuno, and S. Hokamoto, "Position and attitude control of an underactuated satellite with constant thrust," in *AIAA Guidance, Navigation, and Control Conference*, 2011, p. 6352.
- [21] P. Tsiotras and J. Luo, "Control of underactuated spacecraft with bounded inputs," *Automatica*, vol. 36, no. 8, pp. 1153–1169, 2000.
- [22] H. Krishnan, M. Reyhanoglu, and H. McClamroch, "Attitude stabilization of a rigid spacecraft using two control torques: A nonlinear control approach based on the spacecraft attitude dynamics," *Automatica*, vol. 30, no. 6, pp. 1023–1027, 1994.
- [23] P. Crouch, "Spacecraft attitude control and stabilization: Applications of geometric control theory to rigid body models," *IEEE Transactions on Automatic Control*, vol. 29, no. 4, pp. 321–331, 1984.
- [24] F. Bullo, R. M. Murray, and A. Sarti, "Control on the sphere and reduced attitude stabilization," *IFAC Proceedings Volumes*, vol. 28, no. 14, pp. 495–501, 1995.
- [25] R. M. Murray, Z. Li, and S. S. Sastry, *A mathematical introduction to robotic manipulation*. CRC press, 2017.
- [26] A. Diouf, B. Belzile, M. Saad, and D. St-Onge, "Spherical rolling robots—design, modeling, and control: A systematic literature review," *Robotics and Autonomous Systems*, p. 104657, 2024.
- [27] A. Halme, T. Schonberg, and Y. Wang, "Motion control of a spherical mobile robot," in *Proceedings of 4th IEEE International Workshop on Advanced Motion Control-AMC'96-MIE*, vol. 1. IEEE, 1996, pp. 259–264.
- [28] A. Bicchi, A. Balluchi, D. Prattichizzo, and A. Gorelli, "Introducing the 'sphericle': an experimental testbed for research and teaching in nonholonomy," in *Proceedings of International Conference on Robotics and Automation*, vol. 3. IEEE, 1997, pp. 2620–2625.
- [29] Q. Zhan, Y. Cai, and C. Yan, "Design, analysis and experiments of an omni-directional spherical robot," in *2011 IEEE International Conference on Robotics and Automation*. IEEE, 2011, pp. 4921–4926.
- [30] M. Bujňák, R. Pirník, K. Rástočný, A. Janota, D. Nemeč, P. Kuchár, T. Tichý, and Z. Łukasik, "Spherical robots for special purposes: a review on current possibilities," *Sensors*, vol. 22, no. 4, p. 1413, 2022.
- [31] J. Li, S. Jin, C. Wang, J. Xue, and X. Wang, "Weld line recognition and path planning with spherical tank inspection robots," *Journal of Field Robotics*, vol. 39, no. 2, pp. 131–152, 2022.
- [32] J. Okamoto, V. Grassi, P. F. S. Amaral, B. G. M. Pinto, D. Pipa, G. P. Pires, and M. V. M. Martins, "Development of an autonomous robot for gas storage spheres inspection," *Journal of Intelligent & Robotic Systems*, vol. 66, pp. 23–35, 2012.
- [33] F. Luca, G. Robustelli, M. Conforti, and D. Fabbriatore, "Geomorphological map of the crotona province (calabria, south italy)," *Journal of Maps*, vol. 7, no. 1, pp. 375–390, 2011.
- [34] T. Caruso, J. R. Powell, and M. C. Rillig, "Compositional divergence and convergence in local communities and spatially structured landscapes," *PLoS One*, vol. 7, no. 4, p. e35942, 2012.
- [35] D. P. Kumar, S. Darbha, S. G. Manyam, D. W. Casbeer, and M. Pachter, "Equivalence of dubins path on sphere with geographic coordinates and moving frames," *Journal of Guidance, Control, and Dynamics*, pp. 1–6, 2024.

- [36] V. Jurdjevic, *Geometric control theory*. Cambridge university press, 1997.
- [37] D. E. Chang, "A simple proof of the pontryagin maximum principle on manifolds," *Automatica*, vol. 47, no. 3, pp. 630–633, 2011.